Journal of Materials Chemistry A

PAPER

View Article Online
View Journal | View Issue

Cite this: J. Mater. Chem. A, 2018, 6, 7693

Three-step cascade over a single catalyst: synthesis of 5-(ethoxymethyl)furfural from glucose over a hierarchical lamellar multi-functional zeolite catalyst†

Yuanyuan Bai,[abc] Lu Wei,[ad] Mengfei Yang,[e] Huiyong Chen,[e] Scott Holdren,[f] Guanghui Zhu,[g] Dat T. Tran,[h] Chunli Yao,[c] Runcang Sun,[c] Yanbo Pan[i] and Dongxia Liu*[a]

Received 5th February 2018
Accepted 6th March 2018

DOI: 10.1039/c8ta01242c

rsc.li/materials-a

The synthesis of hierarchical lamellar zeolites with a controlled meso-/microporous morphology and acidity is an expanding area of research interest for a wide range of applications. Here, we report a one-step synthesis of a hierarchical meso-/microporous lamellar MFI–Sn/Al zeolite (*i.e.*, containing both Lewis acidic Sn- and Al-sites and a Brønsted acidic Al–O(H)–Si site) and its catalytic application for the conversion of glucose into 5-(ethoxymethyl)furfural (EMF). The MFI–Sn/Al zeolite was prepared with the assistance of a diquaternary ammonium ($[C_{22}H_{45}–N^+(CH_3)_2–C_6H_{12}–N^+(CH_3)_2–C_6H_{13}]Br^{2-}$, $C_{22\text{-}6\text{-}6}$) template in a composition of $100SiO_2/5C_{22\text{-}6\text{-}6}/18.5Na_2O/xAl_2O_3/ySnO_2/2957H_2O$ (x = 0.5, 1, and 2; y = 1 and 2, respectively). The MFI–Sn/Al zeolites innovatively feature dual meso-/microporosity and dual Lewis and Brønsted acidity, which enabled a three-step reaction cascade for EMF synthesis from glucose in ethanol solvent. The reaction proceeded *via* the isomerization of glucose to fructose over Lewis acidic Sn sites and the dehydration of fructose to 5-hydroxymethylfurfural (HMF) and then the etherification of HMF and ethanol to EMF over the Brønsted acidic Al–O(H)–Si sites. The co-existence of multiple acidities in a single zeolite catalyst enabled one-pot cascade reactions for carbohydrate upgrading. The dual meso-/microporosity in the MFI–Sn/Al zeolites facilitated mass transport in processing of bulky biomass molecules. The balance of both types of acidity and meso-/microporosity realized an EMF yield as high as 44% from the glucose reactant.

1 Introduction

Over the past century, the world society has been heavily relying on fossil resources, such as coal, gas, and oil, to produce human beings' daily needed fuels and chemicals.[1–3] The carbon dioxide produced from the usage of these non-renewable fossil resources has been significantly changing the climate on earth,[2] and the heavy reliance on these fossil resources makes them more expensive and less abundant. As a widely available and sustainable carbon source, biomass has the potential to replace non-renewable fossil resources for the production of fuels and chemicals.[4] Lignocellulosic biomass, consisting of 60–80% carbohydrate components,[5] is the most promising renewable carbon source for the production of both fuels and platform chemicals. Many strategies have been explored for the conversion of carbohydrates in lignocellulosic biomass into chemicals and fuels.[6–8] The use of an appropriate catalyst plays a crucial role in achieving high conversion and high selectivity to the end

[a]Department of Chemical and Biomolecular Engineering, University of Maryland, College Park, MD, 20742, USA. E-mail: liud@umd.edu; Fax: +1-301-405-0523; Tel: +1-301-405-3522

[b]National Engineering Lab for Pulp and Paper, China National Pulp and Paper Research Institute Co. Ltd., Beijing, 100102, China

[c]Beijing Key Laboratory of Lignocellulosic Chemistry, Beijing Forestry University, Beijing, 100083, China

[d]College of Materials Science and Engineering, Beijing University of Technology, Beijing 100124, PR China

[e]School of Chemical Engineering, Northwest University, Xi'an, Shaanxi, 710069, China

[f]Department of Chemistry and Biochemistry, University of Maryland, College Park, MD, 20742, USA

[g]School of Chemical and Biomolecular Engineering, Georgia Institute of Technology, Atlanta, Georgia, 30332, USA

[h]U. S. Army Research Laboratory, RDRL-SED-E, 2800 Powder Mill Road, Adelphi, MD, 20783, USA

[i]Department of Chemical and Biomolecular Engineering, University of Akron, Akron 44325, USA

† Electronic supplementary information (ESI) available: Morphological and textural properties of MFI–Sn/Al zeolites; the glucose conversion and product yields *versus* the reaction time over the MFI–Sn/Al zeolite with variable Si/Sn and Si/Al ratios; and the EMF synthesis *versus* the reaction time from different carbohydrate reactants at different reaction temperatures over the MFI–Sn/Al (100/100) zeolite catalyst. See DOI: 10.1039/c8ta01242c

fuel and/or chemical alternative products in a green and economic process.[9,10]

5-(Ethoxymethyl)furfural (EMF), a liquid with a boiling point of 508 K and an energy density of 30.3 MJ L^{-1}, close to that of diesel (33.6 MJ L^{-1}), gasoline (31.1 MJ L^{-1}) and ethanol (23.5 MJ L^{-1}), is an attractive and potential end biofuel alternative product.[11–13] The synthesis of EMF from biomass feedstocks has been practiced *via* a single step etherification of 5-hydroxymethylfurfural (HMF),[14] two-step cascade reaction of dehydration–etherification of fructose,[15] three-step cascade reaction of decomposition–dehydration–etherification of disaccharides (*e.g.*, sucrose)[16] or oligosaccharides (*e.g.*, inulin),[17] and three-step cascade reaction of isomerization–dehydration–etherification of monosaccharides such as glucose[12] in ethanol solvent. The single-step synthesis of EMF from HMF can occur over a variety of acidic catalysts[5] with >90% yield. The high cost and non-stability of HMF, however, restrict its wide application in EMF production. The two-step and three-step cascade reactions of fructose-based feedstocks on acidic catalysts overcome the shortcomings in EMF synthesis *via* the single-step approach, but these saccharides are less abundant in nature. In contrast, glucose or glucose-based oligosaccharides and polysaccharides are the most abundant carbohydrates in lignocellulosic biomass.

The synthesis of EMF from glucose feedstock is desired, but requires multiple types of catalysts for different steps in the reaction cascade. For example, a combination of Sn-BEA and Amberlyst-15 catalysts has been used for glucose conversion to EMF,[12] in which the former catalyst acts as a Lewis acid for the isomerization of glucose to fructose and the latter one catalyzes the dehydration and etherification of fructose to EMF. In this three-step reaction cascade, transport of reaction intermediates from one catalyst to the other in the reactor is needed, which might impede the EMF production efficiency from the process point of view. The usage of multiple catalysts also complicates the catalyst preparation and/or separation steps if catalyst recycling is needed. Multifunctional catalysts, *i.e.*, a single catalyst comprised of structurally and/or compositionally different active components within nanoscale distances, can enable multiple reaction steps successively and efficiently in the catalysis cascade. The precise position of active centers in multifunctional catalysts, like enzymatic catalyst systems in nature,[18–20] can also facilitate cooperative catalysis. The synthesis of EMF from glucose or glucose-based abundant carbohydrates desirably takes place over such a multifunctional catalyst, but such a catalyst system has rarely been reported.

In the present study, we report a hierarchical lamellar multifunctional MFI–Sn/Al zeolite catalyst that contains dual meso-/microporosity and dual Lewis and Brønsted acidity for glucose conversion into the EMF product. The MFI–Sn/Al catalyst was prepared *via* a single-step hydrothermal crystallization method with the assistance of a diquaternary ammonium template ($[C_{22}H_{45}–N^+(CH_3)_2–C_6H_{12}–N^+(CH_3)_2–C_6H_{13}]Br^{2-}$, $C_{22\text{-}6\text{-}6}$) in a composition of $100SiO_2/5C_{22\text{-}6\text{-}6}/18.5Na_2O/xAl_2O_3/ySnO_2/2957H_2O$ ($x = 0.5$, 1, and 2, $y = 1$ and 2, respectively). The co-existence of Sn and Al elements in the MFI–Sn/Al zeolite provides both Lewis acidic Sn- and Al-sites and Brønsted acidic Al–O(H)–Si sites for the three-step reaction cascade of isomerization–dehydration–etherification in the EMF production (Scheme 1). The tetravalent Sn site has shown good performance for catalyzing the isomerization of a series of pentose and hexose sugars with activities comparable to biological processes[19,20] by a mechanism similar to enzymatic catalysts.[18] Therefore, the Sn-sites in the MFI–Sn/Al catalyst were used to catalyze the isomerization step in the reaction cascade. The Brønsted acidic Al–O(H)–Si sites catalyze the subsequent dehydration of fructose to HMF and the etherification of HMF to EMF. The presence of hierarchical meso- and microporosity in the MFI–Sn/Al catalyst allows for facile transport of bulky molecules, thereby further improving the catalyst performance in this reaction cascade. A high EMF yield (44%) has been achieved from glucose conversion over the multifunctional MFI–Sn/Al catalyst.

2 Experimental

2.1 Materials

Aluminum isopropoxide ($Al[OCH(CH_3)_2]_3$, 99.99+% purity), tetraethyl orthosilicate (TEOS, 98%), tetrapropylammonium hydroxide (TPAOH, 40 wt%), D(+)-glucose (98%), D-fructose (98%), sucrose (98%) and inulin (98%) were purchased from Alfa Aesar. Tin chloride pentahydrate ($SnCl_4 \cdot 5H_2O$, 98%), sodium hydroxide (NaOH, ≥97.0%), and ammonium nitrate (NH_4NO_3, ≥99.0%) were supplied by Sigma-Aldrich. Deionized (DI) water was used throughout the experiment. A diquaternary ammonium template ($[C_{22}H_{45}–N^+(CH_3)_2–C_6H_{12}–N^+(CH_3)_2–C_6H_{13}]Br_2$, ($C_{22\text{-}6\text{-}6}$)) was synthesized following a method reported by Choi *et al.*[21] and the detailed synthesis procedure has been described in our previous work.[22,23]

2.2 Catalyst preparation

The MFI–Sn/Al zeolite catalysts were synthesized in a one-step hydrothermal crystallization process using the following recipe: $100SiO_2/5C_{22\text{-}6\text{-}6}/18.5Na_2O/xAl_2O_3/ySnO_2/2957H_2O$, where $x = 0.5$, 1, and 2; $y = 1$ and 2, respectively. Typically, the synthesis was started by dissolving 0.41 g NaOH in 11.50 g DI water, followed by

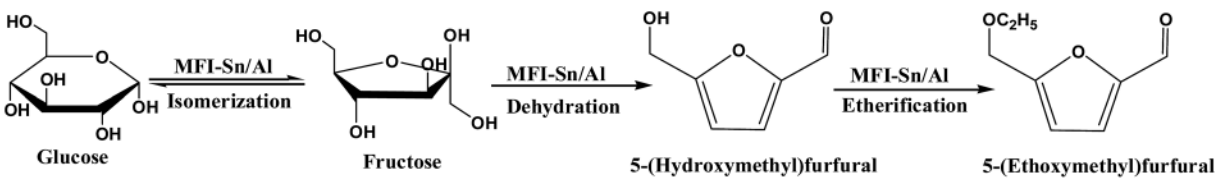

Scheme 1 Schematic illustration of EMF synthesis from glucose *via* a three-step reaction cascade over a single MFI–Sn/Al zeolite catalyst.

the addition of a desired amount of $SnCl_4 \cdot 5H_2O$ and Al $[OCH(CH_3)_2]_3$, separately. After a clear solution was formed, 5.78 g TEOS was added and the resultant mixture was stirred vigorously at room temperature for 8 h. A $C_{22\text{-}6\text{-}6}$ solution was prepared by dissolving 0.95 g $C_{22\text{-}6\text{-}6}$ in 2.83 g of DI water at 333 K and then added into the above mixture. The resultant zeolite synthesis gel was continuously stirred at room temperature for 2 h. Finally, the synthesis gel was transferred into a Teflon vessel in a stainless steel autoclave. The autoclave was tumbled vertically at 30 rpm and 423 K in an oven for 14 days. After the hydrothermal synthesis, the zeolite products were collected by centrifugation at 6000 rpm for 15 min and then washed by dispersing in DI water. The water washing and centrifugation steps were repeated 6 times. A vacuum oven was utilized to dry the wet zeolite product at room temperature overnight. Finally, the zeolite samples were calcined in a flowing air (1.67 mL s^{-1}, ultrapure air, Airgas) at 873 K for 6 h. The obtained samples were named MFI–Sn/Al (Si/Sn molar ratio and Si/Al molar ratio). According to the synthesis recipe, the following samples, MFI–Sn/Al (100/100), MFI–Sn/Al (100/50), MFI–Sn/Al (100/25), MFI–Sn/Al (50/50), and MFI–Sn/Al (∞/100), have been prepared, respectively.

For comparison purposes, the conventional microporous MFI zeolite containing both Sn and Al (designated as C-MFI–Sn/Al (100/100)) was prepared according to the work of Mal *et al.*,[24] and the synthesis procedure is as follows. Firstly, 0.26 g of $SnCl_4 \cdot 5H_2O$ and 0.15 g of $Al[OCH(CH_3)_2]_3$ were dissolved in 19.00 g of DI water in a polyethylene bottle. Then, 15.61 g TEOS was added and the resultant mixture was stirred magnetically for 30 min. 16.50 g TPAOH solution was then added and the mixture was continuously stirred for 1 h. The molar ratio of the C-MFI–Sn/Al (100/100) synthesis gel was $100SiO_2/SnO_2/0.5Al_2O_3/44TPAOH/3430H_2O$. Finally, the mixture was transferred into a Teflon-lined autoclave and kept at 433 K for 2 days under static conditions. After the synthesis, the sample was collected by centrifugation, washed with DI water and calcined using the procedures described for the preparation of MFI–Sn/Al zeolites above.

Prior to catalysis tests, all the zeolite samples were ion-exchanged three times using 1.0 M aqueous NH_4NO_3 solution (weight ratio of zeolite to NH_4NO_3 solution = 1 : 10) for 3 hours at 353 K. The sample was collected by centrifugation, washed with DI water, and dried at 353 K for 12 h. All zeolite samples in their NH_4^+-form were treated in air (1.67 mL s^{-1}, ultrapure air, Airgas) by increasing the temperature from ambient to 823 K at 0.167 K s^{-1} rate and holding them at this temperature for 4 h.

2.3 Catalyst characterization

The scanning electron microscopy (SEM) images taken from a Hitachi Su-70 electron microscope were used to detect the morphologies of the synthesized zeolite samples. The powder X-ray diffraction (XRD) patterns were recorded using a Bruker D8 Advance Lynx Powder Diffractometer (LynxEye PSD detector, sealed tube, Cu Kα radiation with a Ni β-filter) in the 2θ range from 1.2° to 40°. The N_2 adsorption–desorption isotherms were measured at 77 K with an Autosorb-iQ analyzer (Quantachrome Instruments) to characterize the textural properties of the zeolite samples. Prior to the measurements, all the zeolite samples were evacuated overnight at 623 K and 1 mmHg pressure. The solid state magic angle spinning NMR (MAS NMR) spectra were recorded at a field of 7 T (Bruker DSX 300) for ^{29}Si and ^{27}Al. ^{29}Si MAS NMR spectra were recorded at 59.64 MHz using 4 mm rotors at a spinning speed of 10 kHz, a dwell time of 20 μs, a $\pi/2$ pulse of 5.0 μs, and a recycle delay of 60 s. The spectra were referenced with respect to 3-(trimethylsilyl)-1-propanesulfonic acid salt. ^{27}Al MAS NMR spectra were recorded at 78.22 MHz using 4 mm rotors at 10 kHz spinning speed, a dwell time of 1.0 μs, a selective $\pi/10$ pulse of 0.6 μs, and a recycle delay of 4 s. An aqueous solution of aluminum nitrate (0.1 M) was used as the reference. Ultraviolet-visible diffuse reflectance spectroscopy (UV-Vis-DRS) was performed using a Perkin-Elmer Lambda 650S model to understand the structure of the Sn-sites in zeolite samples. The integrating sphere is 60 mm and is made by LabSphere. The coating in the LabSphere 60 mm integrating attachment is Spectrolong. The typical scan rate was 1 nm per second and the scan range was from 200 nm to 800 nm. All the spectra were recorded under ambient conditions.

2.4 Composition and acidity measurements

The Si, Al, and Sn contents of zeolite samples were determined by inductively coupled plasma atomic emission spectroscopy (ICP-AES, iCAP 6500 dual view). The concentration of active Brønsted acid sites in each zeolite sample was determined *via* the reactive gas chromatography (RGC) method using isopropylamine ($CH_3CH(NH_2)CH_3$) as the probe molecule. The selective decomposition of the isopropylamine adsorbate on the Brønsted acid site ($CH_3CH(NH_2)CH_3\cdots AlO(H)Si$) in zeolites *via* Hoffmann elimination forms propylene and ammonia, $CH_3CH(NH_2)CH_3 + AlO(H)Si \rightarrow CH_3CH(NH_2)CH_3\cdots AlO(H)Si \rightarrow CH_2{=}CHCH_3 + NH_3 + AlO(H)Si$.[25,26] The quantification of propylene using a GC instrument determined the number of AlO(H)Si sites in each zeolite sample. The experimental setup and reaction conditions for the chemical titration of the Brønsted acid site were the same as those reported by Abdelrahman *et al.*[26]

The types of acid sites were identified using the Fourier transform infrared (FTIR) spectra recorded on a Nicolet iS-50R spectrometer with an associated Harrick Scientific Praying Mantis optical accessory and high temperature reaction chamber (HVC-DRP-5). In a typical run, the DRIFTS sample cell was filled with a zeolite sample that was pre-treated at 823 K for 6 h under flowing helium (He, 0.083 mL s^{-1}) in a furnace. The zeolite sample was then activated at 823 K under the He flow (0.083 mL s^{-1}) for 1 h in the DRIFTS cell. After cooling the sample to 393 K, a spectrum was recorded against the background spectrum of the KBr powder measured under the same conditions. Afterwards, the adsorption of pyridine was performed by flowing a mixed pyridine and He gas stream through the catalyst. Following the adsorption, the sample was heated to 523 K under flowing He to desorb the physisorbed pyridine, and cooled to a temperature of 393 K, and then FTIR spectra were

recorded in the range of 4000–600 cm^{-1} with 128 scans at an effective resolution of 2 cm^{-1}. The as-recorded FTIR spectra of the adsorbed pyridine were used to determine the type and concentration of Brønsted and Lewis acid sites in the catalyst. Alternatively, the activated zeolite sample in the DRIFT cell was cooled to 303 K and then exposed to a mixed trideuteroacetonitrile (CD_3CN) and argon (Ar) gas stream using a bubbler with Ar as the carrier gas. After the excess CD_3CN was flushed out from the zeolite sample using a flowing Ar gas (0.083 mL s^{-1}), the spectra were collected at 4 cm^{-1} resolution. The recorded FTIR spectra of CD_3CN were used to analyze the Sn-sites in each zeolite sample.

The acidity of the zeolite was further evaluated by ammonia temperature programmed desorption (NH_3-TPD) using an Autosorb-iQ instrument (Quantachrome, ASIQM000-4) equipped with a thermal conductivity detector (TCD). In the NH_3-TPD measurement, the zeolite sample (0.10 g) was loaded into a quartz cell and heated to 873 K at a rate of 0.05 K s^{-1} under He (0.67 mL s^{-1}) and maintained at this temperature for 1 h. After cooling to 423 K under the He stream, the sample was exposed to the NH_3 stream (0.5 mL s^{-1}, ultrapure, Airgas) for 0.5 h, and then back to the helium flow (0.5 mL s^{-1}) for 2 h to remove the NH_3 residue in the system. Lastly, the catalyst sample was ramped to 823 K at a ramp rate of 0.167 K s^{-1}, and the NH_3 desorption profile was recorded.

2.5 Catalytic reaction for EMF synthesis from carbohydrates

In a typical catalytic reaction, a 20 mL thick-walled glass reactor sealed with crimp tops (PTFE/silicone septum) was charged with glucose (0.090 g), the zeolite catalyst (0.074 g), and ethanol (3 mL), respectively. The glass reactor was then heated to a desired temperature and the magnetic stirring was controlled at 600 rpm in all the catalysis experiments. After a certain reaction time, the reactor was quenched in an ice bath and the reaction mixture was sampled for composition analysis. A high performance liquid chromatograph (HPLC, Agilent 1100) equipped with an Aminex HPX-87H column connected to an auto-sampler and a refractive index detector was used to calibrate and separate the reactants and products. During the measurements, the column was kept at 413 K with 0.005 M sulfuric acid at a flow rate of 0.5 mL min^{-1} as the mobile phase. For comparison purposes, the same reaction and composition analysis conditions were applied to the fructose, sucrose, and inulin reactants in ethanol solvent, respectively. The effect of types of reactants on the EMF production over MFI–Sn/Al zeolite catalysts was thus examined.

3 Results and discussion

3.1 Morphological and textural properties of MFI–Sn/Al zeolite catalysts

Fig. 1 shows the XRD patterns of the synthesized hierarchical lamellar MFI–Sn/Al zeolite catalysts. For comparison purposes, the XRD patterns of lamellar MFI that only contains Al sites (MFI–Sn/Al (∞/100)) and conventional microporous MFI that comprises both Sn and Al sites (C-MFI–Sn/Al (100/100)) are included. As indicated in Fig. 1, all the MFI–Sn/Al zeolite samples exhibit similar diffraction patterns, resembling the characteristics of crystalline MFI zeolites.[21,27,28] This result confirms the successful synthesis of hierarchical lamellar MFI in the presence of both Sn and Al species in the synthesis gels. The absence of small-angle diffraction peaks in Fig. 1 suggests that long-range ordering of the layered zeolitic structure does not exist in the hierarchical lamellar MFI–Sn/Al zeolites. A comparison of the peak intensity between the MFI–Sn/Al samples and C-MFI–Sn/Al (100/100) shows that the diffraction peak intensities of the former samples are all relatively lower than that of the latter one. This is mainly caused by the small framework thickness along the *b*-axis direction in the hierarchical lamellar MFI–Sn/Al zeolites compared to that in the three-dimensional microporous C-MFI–Sn/Al (100/100) zeolite.[20]

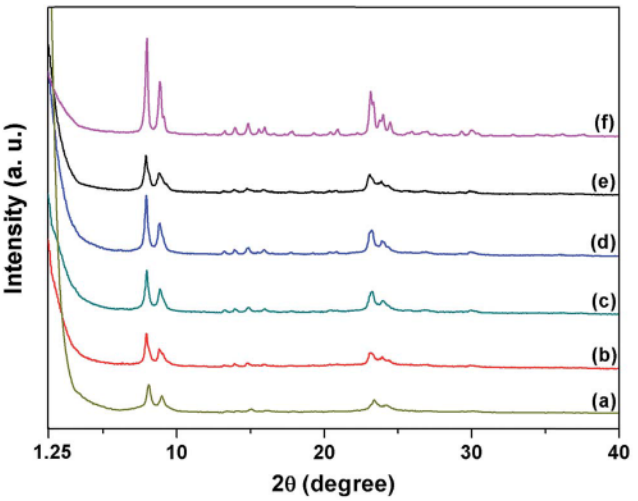

Fig. 1 XRD patterns of (a) MFI–Sn/Al (∞/100), (b) MFI–Sn/Al (50/50), (c) MFI–Sn/Al (100/25), (d) MFI–Sn/Al (100/50), (e) MFI–Sn/Al (100/100) and (f) C-MFI–Sn/Al (100/100).

The morphologies of the hierarchical lamellar MFI–Sn/Al zeolites together with C-MFI–Sn/Al (100/100) and MFI–Sn/Al (∞/100) samples are shown in the SEM images in Fig. 2 and S1 in the ESI.† All the MFI–Sn/Al zeolites (Fig. 2a–e) are comprised of interwoven platelet-like structures that formed flower-like aggregates with irregular sizes (Fig. S1†), while the C-MFI–Sn/Al (100/100) sample is composed of uniform but irregularly shaped particles, whose sizes are in the range of 150–200 nm (Fig. 2f). A closer examination of the MFI–Sn/Al zeolite samples shows that the width and thickness of the platelet-like structure decreases with increasing Al content in the synthesis recipe (Fig. 2a–c). Moreover, the platelet-like structures change from curved to straight ones with increasing Al content. Similarly, the increase in Sn content in the synthesis recipe decreases the thickness of the zeolite platelet-like structure in the MFI–Sn/Al samples (refer to Fig. 2b–d). The effect of Si/Al and Si/Sn ratios in the synthesis recipe on the morphology of derived MFI–Sn/Al zeolites is the same as that observed by Machoke *et al.*[29] on the synthesis of multilamellar MFI under static conditions. The introduction of aluminum and/or tin into

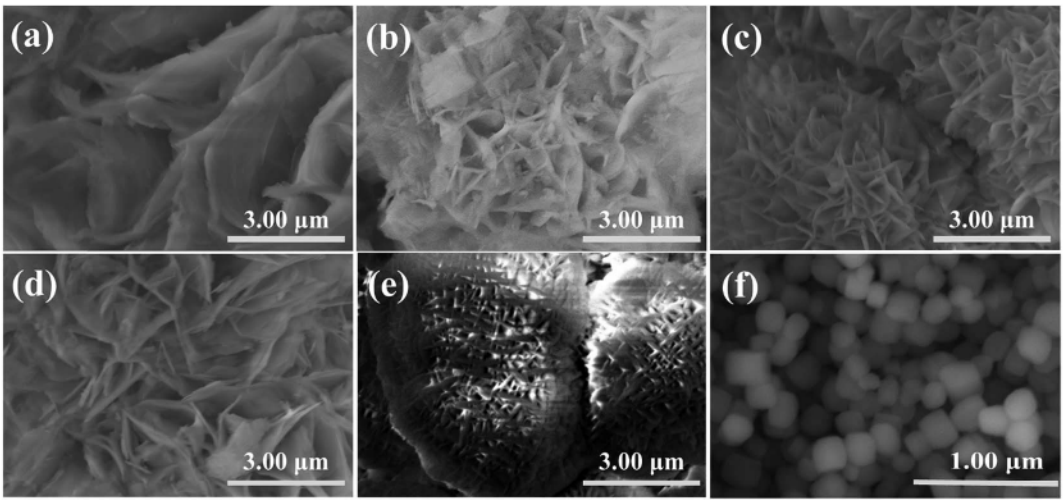

Fig. 2 SEM images of (a) MFI–Sn/Al (100/100), (b) MFI–Sn/Al (100/50), (c) MFI–Sn/Al (100/25), (d) MFI–Sn/Al (50/50), (e) MFI–Sn/Al (∞/100) and (f) C-MFI–Sn/Al (100/100).

the lamellar zeolite synthesis recipe leads to defects in zeolite nanosheet structures, which consequently affect the growth of nanosheets along the *a–c* plane. Therefore, more randomly oriented and smaller sized zeolite nanosheets are formed in the crystallization process, which result in thinner and straighter zeolite plates from the synthetic gels containing higher aluminum and/or tin contents.

N_2 adsorption–desorption isotherms were used to study the textural properties of the MFI–Sn/Al zeolite samples. The textural parameters of each sample are included in Table S1 of the ESI.† Fig. 3A illustrates that all the synthesized hierarchical lamellar MFI–Sn/Al zeolites exhibit type-IV isotherms with hysteresis loops corresponding to capillary condensation in mesopores.[21,30] Particularly, at low relative pressures (P/P_0 < 0.45), the isotherms of these zeolites are similar and comparable to that of the C-MFI–Sn/Al (100/100) zeolite. This suggests that all the synthesized MFI–Sn/Al samples have similar micropore structures. At high relative pressures (P/P_0 > 0.45), the isotherms of the MFI–Sn/Al samples show hysteresis loops, different from that of C-MFI–Sn/Al (100/100). For all the MFI–Sn/Al samples, the hysteresis loops in their isotherms are relatively narrow and flat, which indicates that these materials have disordered mesopores and broad pore size distributions.[31,32] Fig. 3B shows the nonlocal density functional theory (NLDFT) pore size distributions of all MFI–Sn/Al samples. As suggested from the shape of hysteresis loops in their isotherms, the MFI–Sn/Al (100/100), MFI–Sn/Al (50/50), MFI–Sn/Al (100/50), and MFI–Sn/Al (100/25) zeolites have broad mesopore size distributions. In contrast, the C-MFI–Sn/Al (100/100) zeolite does not have significant mesoporosity.

Solid state NMR was employed to investigate the local bonding environment of Si and Al species in the MFI–Sn/Al zeolite catalysts. Fig. 4A and B show the ^{29}Si single pulse (SP) and ^{27}Al NMR spectra of the MFI–Sn/Al (100/100), MFI–Sn/Al (50/50), MFI–Sn/Al (100/50), and MFI–Sn/Al (100/25) zeolites, respectively. In Fig. 4A, one well-resolved peak at −113 ppm and

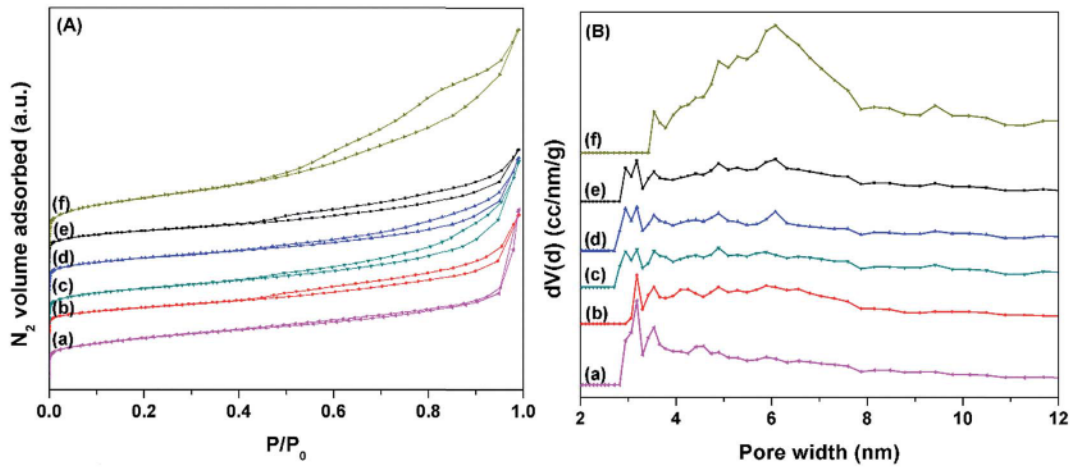

Fig. 3 N_2 isotherms (A) and the corresponding NLDFT pore size distributions (B) as determined from the adsorption branch of (a) C-MFI–Sn/Al (100/100), (b) MFI–Sn/Al (50/50), (c) MFI–Sn/Al (100/25), (d) MFI–Sn/Al (100/50), (e) MFI–Sn/Al (100/100) and (f) MFI–Sn/Al (∞/100), respectively.

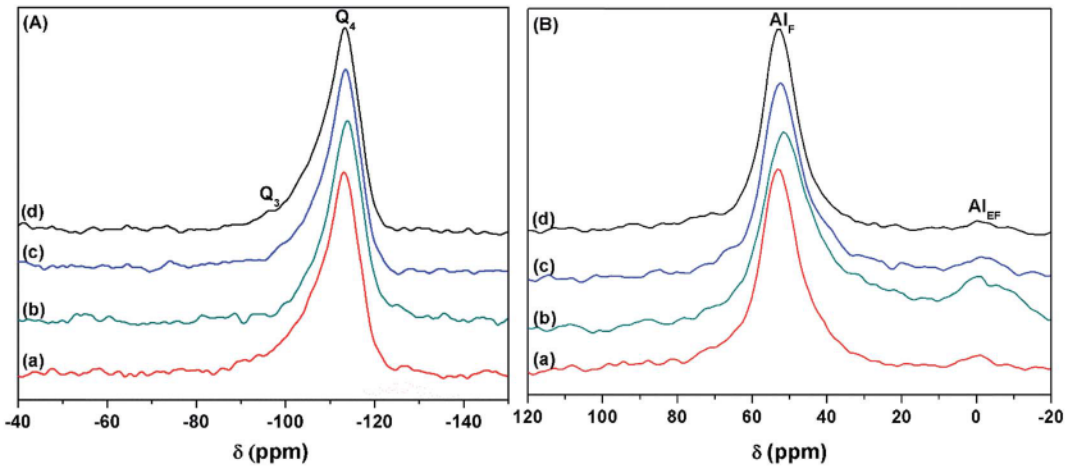

Fig. 4 Solid-state ^{29}Si MAS NMR (A) and ^{27}Al MAS NMR (B) spectra of hierarchical lamellar MFI–Sn/Al zeolite samples: (a) MFI–Sn/Al (50/50), (b) MFI–Sn/Al (100/25), (c) MFI–Sn/Al (100/50), and (d) MFI–Sn/Al (100/100), respectively.

one shoulder peak at −103 ppm can be observed. These two peaks correspond to the crystallographically nonequivalent Q^4 tetrahedral sites (Q^n stands for $X_{4-n}Si[OSi]_n$)[33–36] and Q^3 sites that arise from the silanol groups on the zeolite surface,[23,37] respectively. The similarity of the ^{29}Si SP NMR spectra of MFI–Sn/Al zeolites suggests that similar local bonding environments exist in these samples. In Fig. 4B, two peaks (at 55 ppm and 0 ppm) in the ^{27}Al MAS NMR spectra were observed. The peak at 55 ppm is due to the tetrahedrally coordinated framework aluminum (Al_F), whereas the peak around 0 ppm is due to an octahedral coordination typical of extra-framework Al (Al_{EF}).[38–40] The percentages of the Al_{EF} sites in MFI–Sn/Al (50/50), MFI–Sn/Al (100/25), MFI–Sn/Al (100/50), and MFI–Sn/Al (100/100) samples were calculated from the intensities of the peak around 0 ppm over the peak around 55 ppm, which are 3.6%, 8.1%, 4.4% and 2.0%, respectively. Obviously, the higher Al content in the synthesis led to higher proportions of Al_{EF} in MFI–Sn/Al zeolites. When the concentration of Al was the same, the one with higher Sn content in the synthesis recipe resulted in a higher proportion of Al_{EF} in the as-obtained MFI–Sn/Al samples.

3.2 Composition and acidity of MFI–Sn/Al zeolite catalysts

The tin (Sn) and aluminum (Al) contents of the MFI–Sn/Al zeolite samples were analyzed using the ICP-AES technique, represented by Si/Sn and Si/Al ratios, as shown in Table S2 of the ESI.† The Sn and Al concentrations of the synthesized MFI–Sn/Al samples are generally higher than those determined from the synthesis recipe. Table 1 lists the concentrations of Al and Sn sites determined by elemental analysis and the concentration of Brønsted acid sites measured by the RGC method. The concentration of Al sites is higher than that of Brønsted acid sites, suggesting that there is a considerable amount of non-framework Al in the synthesized MFI–Sn/Al zeolite samples. If we assume all the Al species that could not be detected by the RGC method as Lewis acid sites ($L_{(Al)}$), the ratio of the Brønsted to Lewis (Al) acid sites can be calculated, as shown by entry 6 in Table 1. The overall Brønsted to Lewis acid site ratio (entry 7 in Table 1) in each zeolite sample can also be evaluated by division of Brønsted acid sites by the sum of Lewis (Al) acid and Sn sites. Apparently, the increase in the Al or Sn content in the hydrothermal synthesis gave more Lewis acid sites compared to Brønsted acid sites in the MFI–Sn/Al samples.

Table 1 Concentration of Sn, Al and acid sites in MFI–Sn/Al zeolite catalysts

Zeolite	Sn[a] (mmol g^{-1})	Al[a] (mmol g^{-1})	Brønsted acid site[b] (mmol g^{-1})	Lewis (Al) acid site ($L_{(Al)}$)[c], (mmol g^{-1})	Brønsted/Lewis (Al) acid site ratio[d] ($I_B/I_{L(Al)}$)	Brønsted/Lewis (Al + Sn) acid site ratio[e] ($I_B/I_{L\ (Al+Sn)}$)	Brønsted/Lewis acid site ratio[f] (I_B/I_L)
MFI–Sn/Al (100/100)	0.219	0.245	0.141	0.104	1.351	0.436	0.989
MFI–Sn/Al (100/50)	0.317	0.505	0.239	0.266	0.895	0.410	0.893
MFI–Sn/Al (100/25)	0.299	0.794	0.274	0.520	0.528	0.334	0.744
MFI–Sn/Al (50/50)	0.523	0.438	0.121	0.317	0.379	0.144	0.464
MFI–Sn/Al (∞/100)	0	0.228	0.159	0.069	—	—	—

[a] Calculated from elemental analysis (ICP-AES). [b] Determined from RGC by the selective decomposition of isopropyl amine on Brønsted acid sites. [c] Determined from the deduction of the concentration of Brønsted acid sites determined by RGC from the Al concentration measured by elemental analysis. [d] Calculated by the ratio of data in column 4 relative to that in column 5. [e] Calculated by the ratio of data in column 4 relative to the sum of data in columns 2 and 5. [f] Evaluated by FITR spectra of adsorbed pyridine. I_B/I_L is the ratio of peak intensity of 1545 cm^{-1} relative to that of 1450 cm^{-1}.

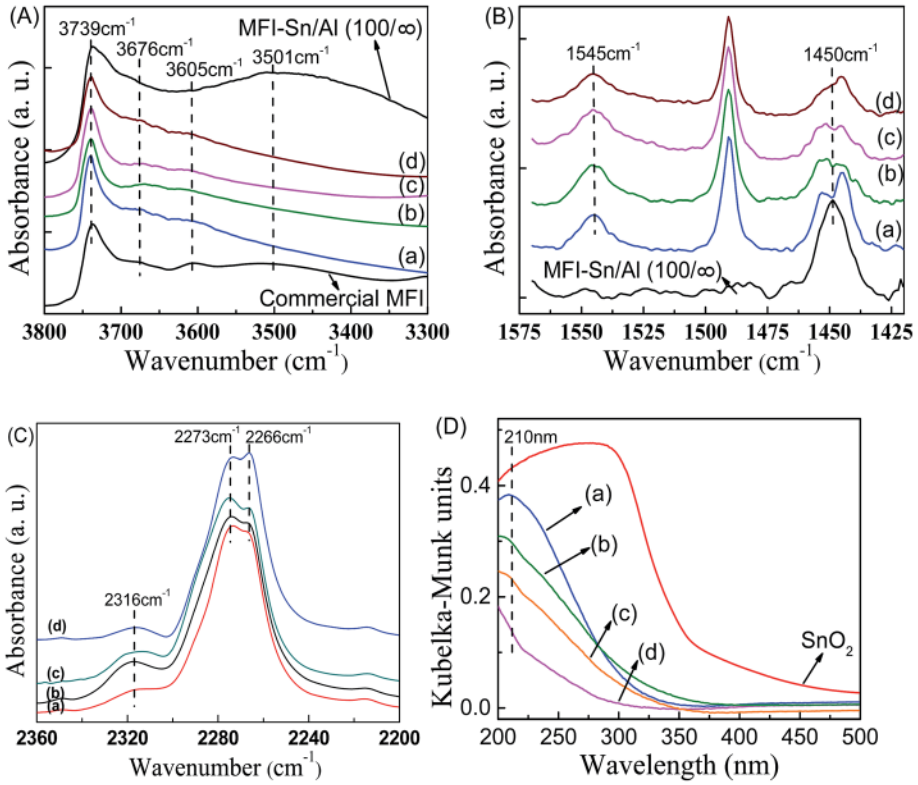

Fig. 5 (A) DRIFTS spectra of MFI–Sn/Al zeolites; FTIR spectra of pyridine (B) and deuterated acetonitrile (C) adsorbed on the MFI–Sn/Al zeolites; and (D) DR-UV-vis spectra of MFI–Sn/Al samples, respectively. (Denotation in each figure: (a) MFI–Sn/Al (50/50), (b) MFI–Sn/Al (100/25), (c) MFI–Sn/Al (100/50) and (d) MFI–Sn/Al (100/100). MFI–Sn/Al (100/∞) stands for conventional microporous MFI comprised of only Sn sites. The commercial MFI with a Si/Al ratio of 40 (Supplier no. 45882-36) in (A) and SnO_2 (Supplier no. 44606-18) in (D) were purchased from Alfa Aesar.)

To understand the types of acidity, the FTIR spectra of the OH-stretching mode (ν(OH)) and adsorbed pyridine in the MFI–Sn/Al samples were recorded, as presented in Fig. 5A and B, respectively. In Fig. 5A, there are four peaks centered around 3739 cm^{-1}, 3676 cm^{-1}, 3605 cm^{-1}, and 3501 cm^{-1}, in sequence, which are associated with terminal silanol (Si–OH) groups, Lewis acidic or non-acidic extra framework Al–OH, Brønsted acid sites (Si–O(H)–Al), and hydrogen-bonded internal silanol (Si–OH) groups.[41–45] In the absence of Al in the MFI–Sn/Al (100/∞) zeolite, the peak of Si–O(H)–Al does not exist, in contrast to the 3605 cm^{-1} peak in all other MFI–Sn/Al samples. The same trend is observed with Al–OH sites in all these samples. The increase in Al (samples (b)–(d)) or Sn (samples (a) and (c)) content increased the Al–OH and (Si–O(H)–Al) sites, as indicated by the increasing intensity of 3676 cm^{-1} and 3605 cm^{-1} peaks. The control sample, commercial MFI, and the conventional microporous MFI–Sn/Al (100/∞) both contain a big peak at 3500 cm^{-1}, indicating the presence of internal Si–OH groups in these samples. The hierarchical MFI–Sn/Al zeolites, apparently, have quite a low amount of such internal groups. Fig. 5B presents the FTIR spectra of adsorbed pyridine on zeolites, which hint at the relative ratio of Brønsted to Lewis acid sites in the MFI–Sn/Al samples.[46] MFI–Sn/Al (50/50), MFI–Sn/Al (100/25), MFI–Sn/Al (100/50) and MFI–Sn/Al (100/100) all showed characteristic peaks for Brønsted (1545 cm^{-1}) and Lewis (1450 cm^{-1}) acid sites. MFI–Sn/Al (100/∞) only showed the peak of Lewis acid sites due to the absence of Al in the structure. The difficulty in determining the accurate molar extinction coefficients of solid acid materials in DRIFT mode restricts our capability of calculating the accurate number of Brønsted and Lewis acid sites in each sample.[47,48] The intensities of the signals in Fig. 5B, due to both types of acid sites, are proportional to their concentrations. Therefore, we conducted semi-quantitative analyses of the ratio of Brønsted to Lewis acid sites in MFI–Sn/Al zeolites by calculating the intensity ratio of Brønsted relative to the Lewis (I_B/I_L) acid sites in these samples. As listed in Table 1, the I_B/I_L decreases with increasing Al content from samples (b)–(d). The increase in Sn content in samples (a) and (c) enhanced the Lewis acidity. These results are consistent with the type of acidity determined by the combination of elemental analysis and RGC measurements in Table 1.

FTIR spectroscopy of adsorbed deuterated acetonitrile can be used for the characterization of the framework and extra-framework Lewis acid Sn sites in Sn-Beta[49,50] or Sn-MFI[51] zeolites. We also used this technique to understand the structure of Sn sites existing in the synthesized MFI–Sn/Al zeolites. As shown in Fig. 5C, three peaks at 2266, 2273 and 2316 cm^{-1} are observed, which are assigned to the C–N stretching vibration of the adsorbed deuterated acetonitrile.[49] The band at 2266 and 2273 cm^{-1} corresponds to the deuterated acetonitrile physisorbed and adsorbed on silanol groups. The band at 2316 cm^{-1} can be assigned to the stronger deuterated

acetonitrile adsorption on Lewis acid sites.[49] According to a previous report,[50] the features near 2316 cm^{-1} are clearly associated with framework Sn sites, which confirmed the presence of framework Sn in the zeolite structures. Furthermore, the structure of Sn sites was evaluated using the UV-vis-DRS spectra, as shown in Fig. 5D. The absorbance around 210 nm was observed for all the MFI–Sn/Al samples, showing the presence of isolated, tetrahedral Sn^{4+} species within the zeolite framework. The increase in the Sn content in the synthesis increased the Sn^{4+} sites in the resultant MFI–Sn/Al zeolites, as indicated by the samples (a) and (c) in Fig. 5D. The increase in Al content in zeolite synthesis affected the incorporation of Sn sites into the framework, as reflected by the increase in 210 nm peak intensity from samples (b)–(d). Apparently, no Sn oxide is observed in all MFI–Sn/Al zeolite samples, as indicated by the absence of the characteristic peak of the SnO_2 sample.

The acidity of the MFI–Sn/Al zeolite catalysts was further characterized by the NH_3-TPD measurements, and the results are shown in Fig. 6. Two desorption peaks located in the temperature range of 400–550 K (low temperature desorption peak) and 550–750 K (high temperature desorption peak), respectively, are observed in all the tested zeolite samples. It has been generally reported that the low temperature peak is associated with the physical and Lewis acid site adsorption of NH_3, while the high temperature desorption peak is assigned to the adsorption of NH_3 onto the Brønsted acid sites in the catalysts[52–54], although caution must be paid since desorption of NH_3 from non-acidic sites in catalysts can take place over a wide temperature range.[55,56] Additionally, the intensity is correlated with the quantity of acid sites in the zeolite catalysts.[57] Fig. 6 shows that the low and high temperature desorption peaks increased with increasing Al sites from MFI–Sn/Al (100/∞), MFI–Sn/Al (100/100), and MFI–Sn/Al (100/50) to MFI–Sn/Al (100/25) materials. The increase in Sn sites mainly increases the low temperature peak, as the zeolite samples transit from MFI–Sn/Al (∞/100) to MFI–Sn/Al (100/100) and MFI–Sn/Al (50/50) to MFI–Sn/Al (100/50). The results suggest that Al in the MFI–Sn/Al zeolites led to both Lewis and Brønsted acidity, while Sn-site predominately contributes to the Lewis acidity.

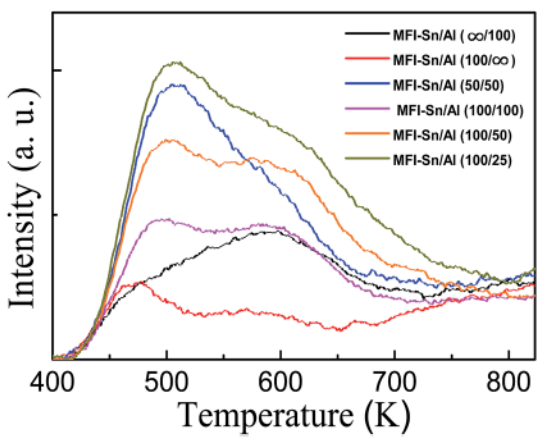

Fig. 6 NH_3-TPD profiles of MFI–Sn/Al zeolites with different Si/Al and Si/Sn ratios. (MFI–Sn/Al (∞/100) and MFI–Sn/Al (100/∞) stand for the conventional microporous MFI zeolites containing only Al and Sn sites, respectively.)

3.3 Reaction cascade for EMF synthesis from carbohydrates over MFI–Sn/Al zeolite catalysts

As shown in Scheme 1, the EMF synthesis from glucose carbohydrate occurs *via* a three-step reaction cascade, in which the first step is the isomerization of glucose into fructose and the next two steps are the dehydration of fructose to HMF and the etherification of HMF to the EMF final product. The first step reaction can be catalyzed by the Lewis acidic Sn sites and the last two steps can take place over the Brønsted acidic Al–O(H)–Si sites in the MFI–Sn/Al zeolite catalysts. The acidity characterization in Section 3.2 indicates the co-existence of both Sn and Al sites, *i.e.*, both Lewis and Brønsted acid sites, in the MFI–Sn/Al zeolites. We expect that they are efficient catalysts for this three-step reaction cascade. Moreover, the morphological and textural property characterization in Section 3.1 indicates the presence of mesoporosity in the synthesized MFI–Sn/Al zeolites, which could be beneficial for the reaction cascade compared to the conventional microporous zeolite analogue. We, therefore, studied the performance of the MFI–Sn/Al zeolite catalysts in EMF synthesis from carbohydrate reactants. The effects of the catalyst structure, reaction temperature, catalyst acidity and carbohydrate reactant type on EMF synthesis were examined in sequence *via* a series of catalytic reactions. The reaction conditions used for EMF synthesis from the glucose reactant over the MFI–Sn/Al (100/100) catalyst at 413 K were used as the base case for comparison. Individual experimental variables were changed, and the effects of changing these variables were investigated by comparing the catalysis data to those obtained under the standard conditions, as discussed below.

3.4 EMF synthesis from glucose over MFI–Sn/Al (100/100), C-MFI–Sn/Al (100/100) and MFI–Sn/Al (∞/100) catalysts

The synthesis of EMF from glucose was carried out over the MFI–Sn/Al (100/100), C-MFI–Sn/Al (100/100), and MFI–Sn/Al (∞/100) zeolite catalysts. Fig. 7a–c show the glucose conversion and product yields *versus* the reaction time over each catalyst. It should be noted that the products are mainly comprised of fructose, HMF and EMF in the glucose-to-EMF conversion, and thus only these major products were analyzed in the present study. Fig. 7d shows the EMF yield at a reaction time of 9 h over each tested catalyst. As demonstrated in Fig. 7a–c, the glucose conversion was higher on MFI–Sn/Al (100/100) than on C-MFI–Sn/Al (100/100), and so was the EMF yield (Fig. 7d). A closer examination of the kinetic data (*e.g.*, reaction time: <5 h) in Fig. 7a and b shows that the EMF formation took place at a much faster rate on MFI–Sn/Al (100/100) than on the C-MFI–Sn/Al (100/100) catalyst. These results indicate that mesoporosity in the hierarchical lamellar MFI zeolite plays an important role in enhancing this three-step reaction cascade. As reported previously, the Stokes diameter of glucose is 0.73 nm,[58] larger than the micropore sizes of MFI zeolites. As a result, the reaction mainly takes place on the external surface of the

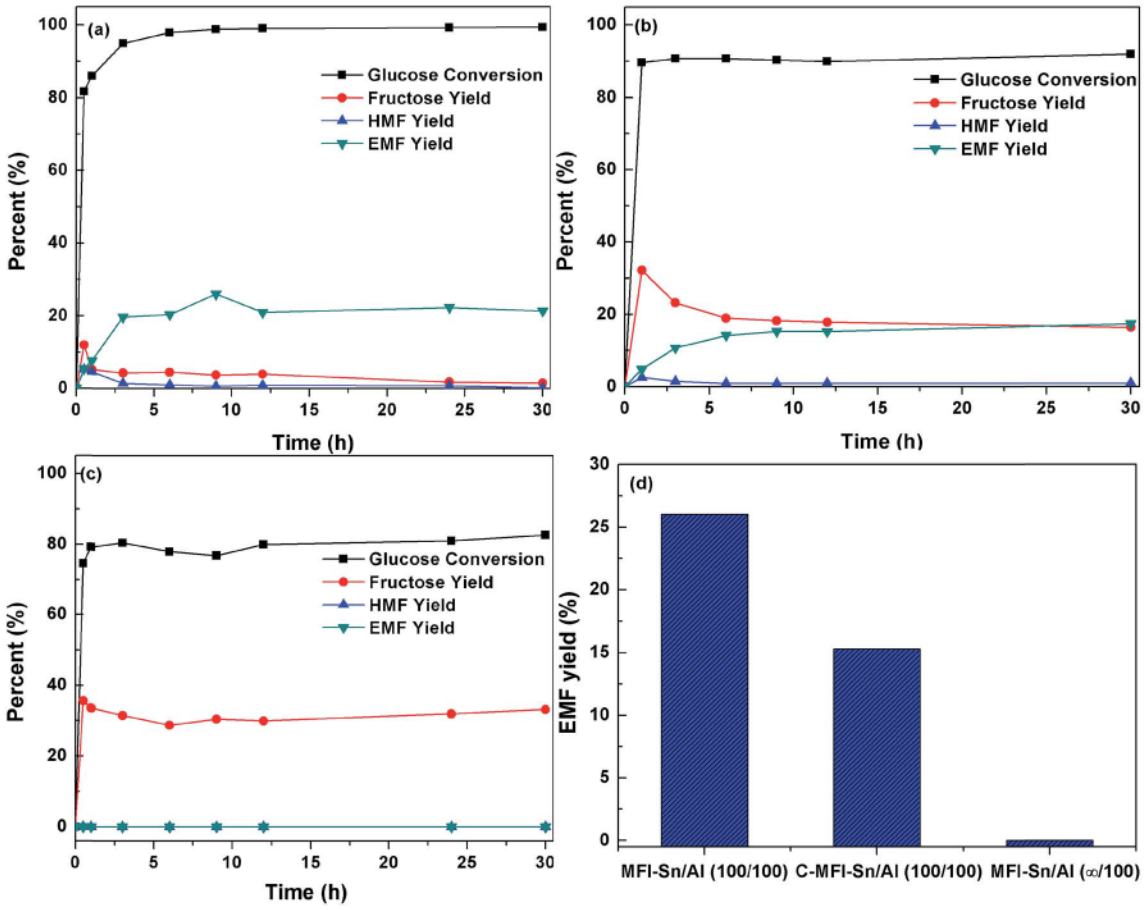

Fig. 7 Catalytic conversion of glucose to EMF over (a) MFI–Sn/Al (100/100), (b) C-MFI–Sn/Al (100/100) and (c) MFI–Sn/Al (∞/100), respectively, *versus* the reaction time. (d) shows the EMF yield at a reaction time of 9 h over these three zeolite catalysts (reaction conditions: glucose: 0.090 g; zeolite: 0.074 g; temperature: 413 K; ethanol: 3 mL).

conventional C-MFI–Sn/Al (100/100) zeolite. The presence of mesopores in MFI–Sn/Al (100/100) apparently promotes the access of the reactant to acid sites in the interior of the MFI–Sn/Al (100/100) zeolite. The mesopores also enhance the transport of the reactant onto or product (or reaction intermediate) away from the active sites in the catalyst in these three steps in the reaction cascade. The sole presence of Al sites in the hierarchical lamellar MFI zeolite (MFI–Sn/Al (∞/100)) also enabled glucose conversion, but the conversion was lower than that of MFI–Sn/Al (100/100) and produced nearly zero EMF (Figs.7c and d). Both glucose conversion and EMF yield suggest the efficiency of Lewis Sn sites in catalysts for glucose isomerization, as well as for the dehydration and etherification steps in the three-step reaction cascade. Additionally, the comparison between the performances of MFI–Sn/Al (100/100) and MFI–Sn/Al (∞/100) also suggests the efficiency of the cooperative catalysis offered from both types of acid sites in this three-step reaction cascade.

3.5 Effect of reaction temperature on EMF synthesis from glucose over the MFI–Sn/Al (100/100) catalyst

The effect of reaction temperature on glucose conversion to EMF over the MFI–Sn/Al zeolite catalysts was examined by employing the MFI–Sn/Al (100/100) catalyst at the reaction temperature of 398 K, 406 K, and 413 K, respectively. Fig. 8 shows the glucose conversion and product yields as a function of the reaction time (Fig. 8a–c) together with the EMF yield at a reaction time of 9 h (Fig. 8d) at these three reaction temperatures. By increasing the reaction temperature from 398 K to 413 K, the rate of glucose conversion increased, so did the fructose conversion and EMF production (refer to reaction times of 0–5 h in Fig. 8a–c). The changes of HMF yields follow the same trend as fructose. This indicates the successive three-step reaction nature of the glucose-to-EMF reaction cascade, besides the endothermic nature of these three reaction steps. The maximum EMF yields in the course of this reaction slightly increased with an increase in the reaction temperature. As shown in Fig. 8d, the EMF yield increased from 23.2% to 24.5% and then to 26.0% when the reaction temperature was increased from 398 K to 406 K and then to 413 K. These results indicate that higher temperature increases the conversion of the glucose reactant and the successive step of dehydration of fructose in the three-step reaction cascade.

3.6 Effect of zeolite acidity on EMF synthesis from glucose over MFI–Sn/Al catalysts

The influences of Sn and Al contents (*i.e.*, acidity, represented by Si/Sn and Si/Al ratios) in MFI–Sn/Al zeolite catalysts on their

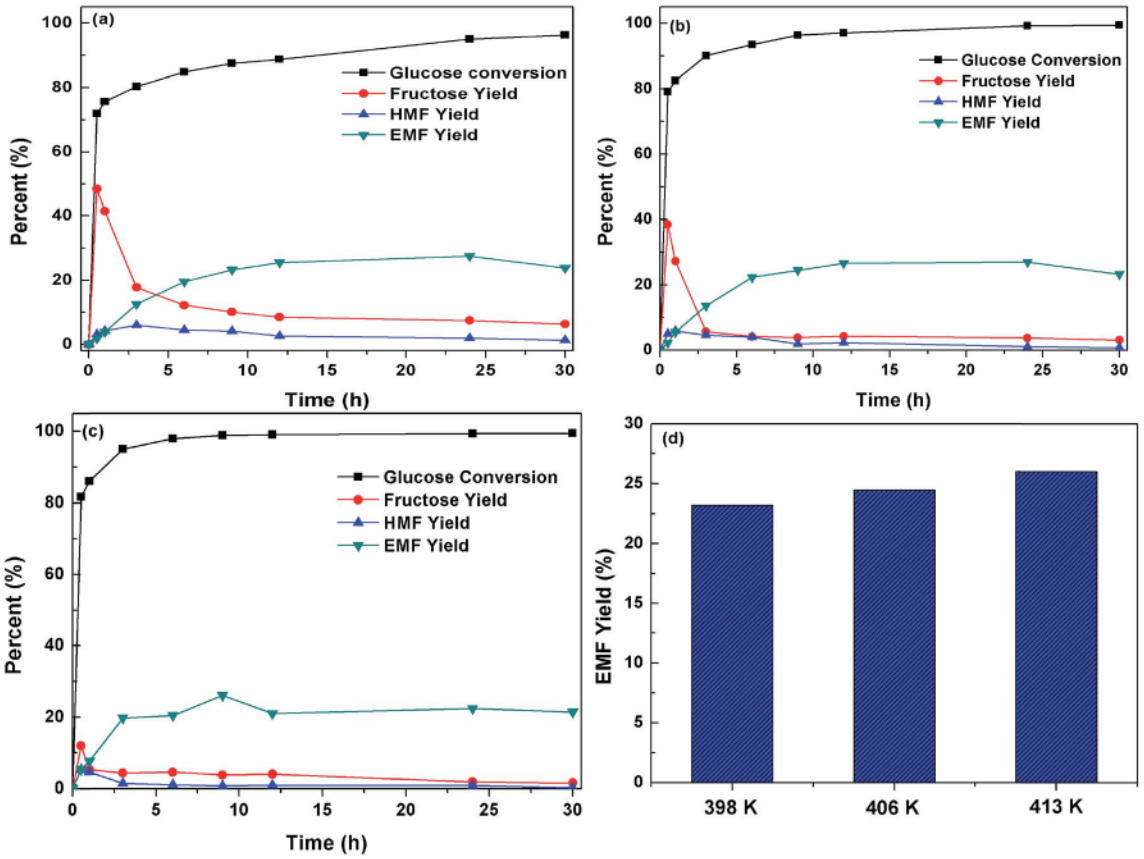

Fig. 8 Effect of reaction temperature ((a) 398 K, (b) 406 K, and (c) 413 K, respectively) on the catalytic conversion of glucose to EMF over MFI–Sn/Al (100/100). (d) shows the maximum EMF yield of the reaction process at these three temperatures (reaction conditions: glucose: 0.090 g; zeolite: 0.074 g; ethanol: 3 mL).

catalytic performances in the glucose-to-EMF reaction were studied at 413 K. Fig. 9 shows the product yields from the reaction over MFI–Sn/Al (100/100), MFI–Sn/Al (100/50), MFI–Sn/Al (100/25), and MFI–Sn/Al (50/50) catalysts, respectively. As indicated in this figure, all the MFI–Sn/Al zeolites enabled EMF, HMF and fructose production. The yields of these three products follow the order of EMF > fructose > HMF in each catalyst, suggesting that the etherification of HMF to EMF happened much faster than the dehydration of fructose in this reaction cascade. Fig. 9 also shows that the HMF and EMF yields of this reaction cascade increase in the order of MFI–Sn/Al (100/100) < MFI–Sn/Al (100/50) < MFI–Sn/Al (100/25) ≪ MFI–Sn/Al (50/50). The fructose yield also follows the same order as that of EMF and HMF over the MFI–Sn/Al (100/100), MFI–Sn/Al (100/50) and MFI–Sn/Al (100/25) catalysts that have a similar number of Sn sites but different Al sites. The increase in Al content increases the Brønsted acidity of the MFI–Sn/Al catalysts, which benefits the etherification of HMF to EMF reaction step. Additionally, this acidity enhances the dehydration of fructose to HMF and isomerization of glucose to fructose reaction steps. It should be noted that the glucose conversion happened at a slower rate with increasing Al content in MFI–Sn/Al catalysts (refer to Fig. S2a–c in Section S2 of the ESI†). The controversy between the glucose conversion and fructose/HMF/EMF formation with

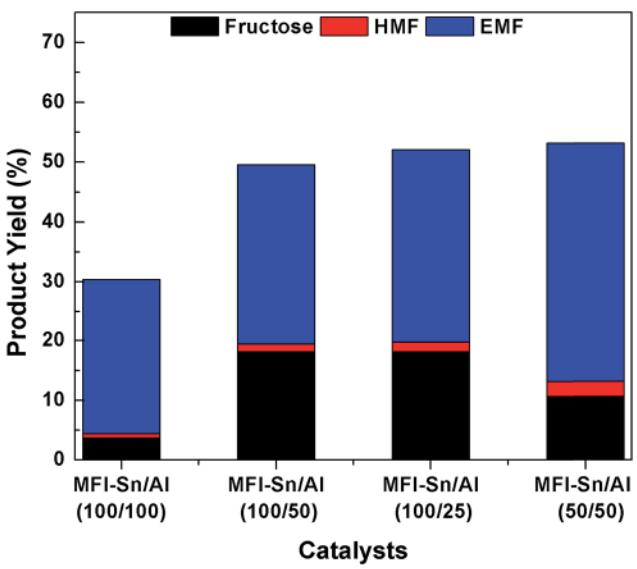

Fig. 9 Effect of Al and Sn contents in hierarchical lamellar MFI–Si/Al zeolites on the conversion of glucose to EMF at 413 K (reaction conditions: glucose: 0.090 g; zeolite: 0.074 g; time: 9 h; ethanol: 3 mL).

increasing Al content in the MFI–Sn/Al catalysts suggests that the increased Brønsted acidity affected the performance of Lewis acidity from Sn sites, *i.e.*, promoted fructose formation from glucose isomerization and suppressed glucose conversion to side products and thus the glucose conversion rate, which overall might be the consequences of cooperative catalysis between both types of acidity in a single catalyst for this three-step reaction cascade.

The comparison of glucose conversion and product yields between the MFI–Sn/Al (100/50) and MFI–Sn/Al (50/50) catalysts in Fig. 9 and S2 (Section S1 in the ESI†) shows the effect of Sn sites (*i.e.*, Lewis acidity) on the performance of the hierarchical lamellar MFI–Sn/Al catalysts. The increase in Sn sites promoted the glucose conversion as well as HMF and EMF formation, while the fructose yield reduced. It is suggested that Sn sites in zeolites function as a Lewis acid that is beneficial for the isomerization of glucose to fructose,[59] and thus higher glucose conversion and fructose formation are expected with increasing Sn sites while keeping the Al site concentration in the MFI–Sn/Al catalysts. The discrepancy between the observed lower fructose formation (or yield) and higher glucose conversion as well as higher HMF and EMF formation in this three-step reaction cascade hints that cooperative catalysis between the Brønsted acidic Al–O(H)–Si sites and Lewis acidic Sn sites might be the reason for these observed catalytic results. The nearly complete conversion of glucose over each catalyst (Section S2 of the ESI†) suggests that Sn sites in each MFI–Sn/Al catalyst are efficient for the isomerization of the glucose reactant in this reaction cascade. Overall, the increase in the Sn or Al content in the catalyst facilitates the particular reaction step in the reaction cascade, which consequently influences the whole reaction network and exhibits different catalytic performances. A good balance between the two types of acid sites can be optimized to realize cooperative catalysis for further optimizing the EMF yield in glucose conversion in the reaction cascade. As shown in Fig. 9, the MFI–Sn/Al (50/50) zeolite showed the best performance, with an EMF yield as high as ~44%, among these four MFI–Sn/Al catalyst formulations.

3.7 Effect of carbohydrate type on EMF synthesis over the MFI–Sn/Al (100/100) catalyst

Glucose is one type of monosaccharide and simple carbohydrate in lignocellulosic biomass, which has shown the feasibility of conversion into EMF over the MFI–Sn/Al zeolite catalysts. In reality, natural biomass produces various types of saccharides, including other monosaccharides, disaccharides and polysaccharides. To investigate the applicability of the hierarchical lamellar MFI–Sn/Al in enabling reaction cascades for the conversion of other types of biomass feedstock into more valuable EMF products, we purposely studied the performance of the MFI–Sn/Al (100/100) catalyst in EMF synthesis from fructose monosaccharide, sucrose disaccharide and inulin polysaccharide (a polymer of ~24 fructose and 1 glucose units), respectively. The effect of temperature on the conversion of these carbohydrate feedstocks for EMF production was also studied. For comparison purposes, the EMF yields from glucose

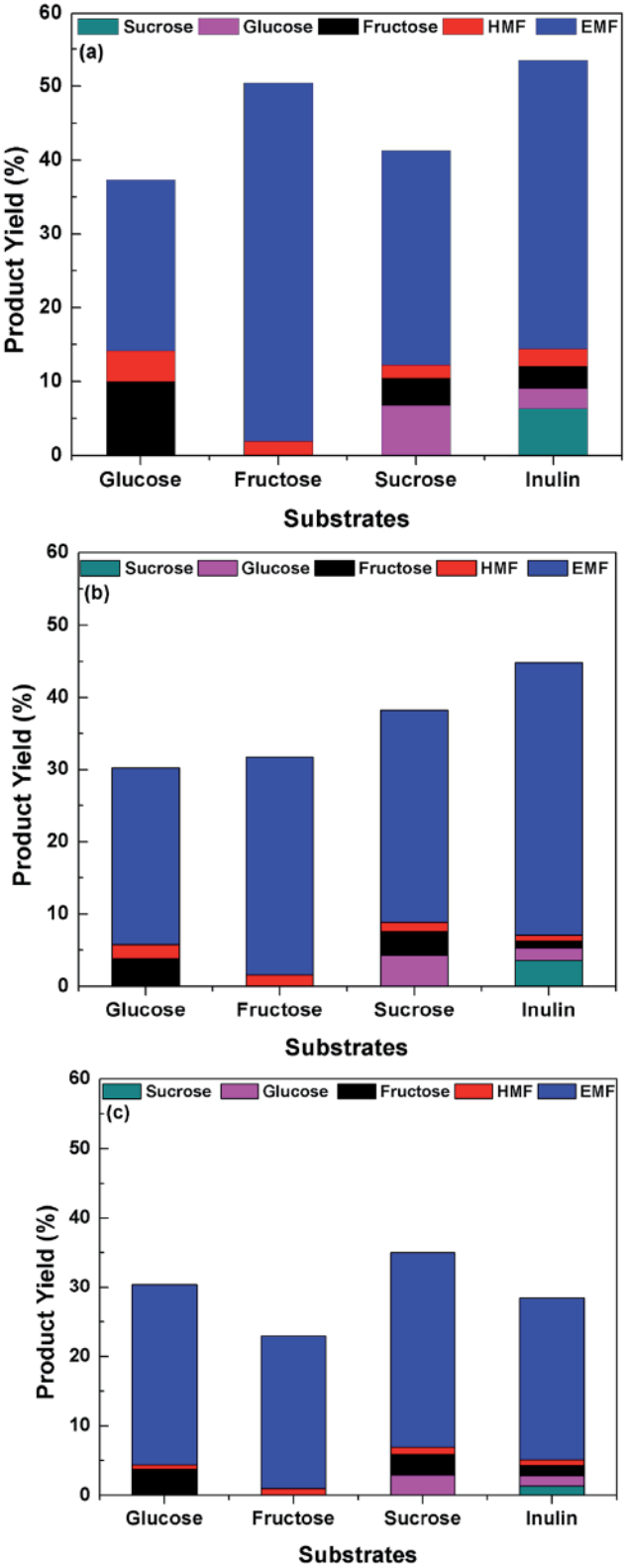

Fig. 10 Effect of carbohydrate reactants on the synthesis of EMF over MFI–Sn/Al (100/100) at a temperature of (a) 398 K, (b) 406 K, and (c) 413 K, respectively (reaction conditions: carbohydrate reactant: 0.090 g; zeolite: 0.074 g; time: 9 h; ethanol: 3 mL).

conversion at different temperatures are included in this section.

Fig. 10 shows product yields from the conversion of different carbohydrates over the MFI–Sn/Al (100/100) catalyst at the temperature of 398 K, 406 K, and 413 K, respectively. As shown in Fig. 10a, the EMF yield at 398 K increases with the reactant changing from glucose, sucrose, inulin, to fructose in sequence. This trend is consistent with the fructose composition of the glucose, sucrose, inulin and fructose carbohydrates. It is known that glucose is a simple monosaccharide; sucrose is a disaccharide that is composed of 1 glucose and 1 fructose units; inulin is a polysaccharide that is comprised of 1 glucose and ~24 fructose units; and fructose is a simple monosaccharide. The formation of EMF from fructose only needs to go through a two-step (dehydration of fructose to HMF and etherification of HMF to EMF) reaction cascade, which eases the reaction network. The increase in fructose units in these four reactants incrementally shifts the reaction cascade from three steps to two steps, and thus leads to a higher EMF yield. It should be noted that reaction intermediates were all observed in these reaction cascades over the MFI–Sn/Al (100/100) catalyst, although EMF is the major product. For example, when sucrose was used as the reactant, the glucose, fructose and HMF reaction intermediates in minor quantities were all observed. This indicates the occurrence of the reaction cascade is effectively enabled by the dual Lewis and Brønsted acidic catalyst. The nearly complete conversion of each carbohydrate reactant and fast reactant conversion rates (see Fig. S3–S5 in Section S3 of the ESI†) indicate that the mass transport limitation is negligible due to the dual meso-/microporosity in the hierarchical lamellar MFI–Sn/Al (100/100) catalyst.

Fig. 10b and c show the product yields from carbohydrate conversion over the MFI–Sn/Al (100/100) catalyst at 406 K and 413 K, respectively. First of all, EMF is still the major product although the total detectable product yields are decreased to different degrees with respect to different reactants with increasing reaction temperature. Specifically, the EMF yield from the glucose reactant slightly increases with the reaction temperature, as discussed above. The EMF yield keeps almost constant from the sucrose reactant, while it decreases significantly with increasing temperature from the fructose and inulin carbohydrate reactants. The changes in EMF yield from different reactants over the MFI–Sn/Al catalyst reveal that higher temperature benefits the isomerization of glucose than the dehydration of fructose and the etherification of HMF to EMF. The decrease in the EMF yield from fructose and inulin may be caused by the increased side reactions along with the reaction cascade with increasing reaction temperature.

4 Conclusions

Hierarchical lamellar MFI–Sn/Al zeolites that comprise dual meso-/microporosity and dual Lewis acidic Sn and Brønsted acidic Al–O(H)–Si sites in single zeolite particles have been successfully prepared. The one-step crystallization of MFI zeolites in the presence of both Sn and Al precursors with the assistance of a diquaternary ammonium template has been simply employed to create this multifunctional MFI–Sn/Al zeolite. The morphological and textural property measurements confirm the presence of mesoporosities in these zeolite catalysts. The acidity characterization shows the existence of dual types of acidity and variations of these acidities with the Si/Al and Si/Sn ratios in the zeolite synthesis recipe. As a consequence of the dual porosity and acidity features, the MFI–Sn/Al zeolites were studied as catalysts for the conversion of glucose into the EMF product in ethanol solvent. The reaction proceeded *via* the isomerization of glucose to fructose over Lewis acidic Sn-sites and the dehydration of fructose to HMF and then the etherification of HMF and ethanol to EMF over the Brønsted acidic Al–O(H)–Si sites. The dual meso-/microporosity in the MFI–Sn/Al zeolites facilitated mass transport in processing of bulky molecules involved in this reaction cascade. The balance between two types of acidities possibly facilitated cooperative catalysis, which led to an EMF yield as high as 44% from the glucose reactant. The co-existence of multiple acidities and porosities in a single zeolite catalyst enabled one-pot cascade reactions for carbohydrate upgrading, which is potentially applicable for processing of other complex reaction networks for efficient production of end chemicals/fuels from renewable biomass resources.

Conflicts of interest

There are no conflicts to declare.

Acknowledgements

The authors gratefully acknowledge the support from the National Science Foundation (NSF-CBET 1642405, 1705284 and 1351384). This work is supported in part by the U. S. Army Research Laboratory (contract/grant number: W911NF-16-2-0036) and the U. S. Army Research Office (contract/grant number: W911NF-17-1-0363). The authors also acknowledge the support of the Maryland NanoCenter and its NispLab. The NispLab is supported in part by the NSF as a MRSEC Shared Experimental Facility. Y. Bai acknowledges the China National Science Foundation (No. 31470605) for financial support for her study at the University of Maryland.

References

1 A. Brandt, J. Gräsvik, J. P. Hallett and T. Welton, *Green Chem.*, 2013, **15**, 550–583.
2 A. J. Ragauskas, C. K. Williams, B. H. Davison, G. Britovsek, J. Cairney, C. A. Eckert, W. J. Frederick, J. P. Hallett, D. J. Leak and C. L. Liotta, *Science*, 2006, **311**, 484–489.
3 R. Xing, A. V. Subrahmanyam, H. Olcay, W. Qi, G. P. van Walsum, H. Pendse and G. W. Huber, *Green Chem.*, 2010, **12**, 1933–1946.
4 A. Demirbaş, *Energy Convers. Manage.*, 2001, **42**, 1357–1378.
5 A. Liu, Z. Zhang, Z. Fang, B. Liu and K. Huang, *J. Ind. Eng. Chem.*, 2014, **20**, 1977–1984.
6 J. B. Binder and R. T. Raines, *J. Am. Chem. Soc.*, 2009, **131**, 1979–1985.

7 J. N. Chheda, G. W. Huber and J. A. Dumesic, *Angew. Chem., Int. Ed.*, 2007, **46**, 7164–7183.
8 Y. Zhang, Z. Xue, J. Wang, X. Zhao, Y. Deng, W. Zhao and T. Mu, *RSC Adv.*, 2016, **6**, 51229–51237.
9 M. Balakrishnan, E. R. Sacia and A. T. Bell, *Green Chem.*, 2012, **14**, 1626–1634.
10 E. Taarning, I. S. Nielsen, K. Egeblad, R. Madsen and C. H. Christensen, *ChemSusChem*, 2008, **1**, 75–78.
11 P. Che, F. Lu, J. Zhang, Y. Huang, X. Nie, J. Gao and J. Xu, *Bioresour. Technol.*, 2012, **119**, 433–436.
12 C. M. Lew, N. Rajabbeigi and M. Tsapatsis, *Ind. Eng. Chem. Res.*, 2012, **51**, 5364–5366.
13 H. Wang, T. Deng, Y. Wang, Y. Qi, X. Hou and Y. Zhu, *Bioresour. Technol.*, 2013, **136**, 394–400.
14 B. Liu, Z. Zhang and K. Huang, *Cellulose*, 2013, **20**, 2081–2089.
15 H. Wang, T. Deng, Y. Wang, X. Cui, Y. Qi, X. Mu, X. Hou and Y. Zhu, *Green Chem.*, 2013, **15**, 2379–2383.
16 Y. Yang, M. M. Abu-Omar and C. Hu, *Appl. Energy*, 2012, **99**, 80–84.
17 Z. Zhang, Y. Wang, Z. Fang and B. Liu, *ChemPlusChem*, 2013, **79**, 233–240.
18 R. Bermejo-Deval, R. S. Assary, E. Nikolla, M. Moliner, Y. Román-Leshkov, S. Hwang, A. Palsdottir, D. Silverman, R. F. Lobo, L. A. Curtiss and M. E. Davis, *Proc. Natl. Acad. Sci. U. S. A.*, 2012, **109**, 9727–9732.
19 E. Nikolla, Y. Román-Leshkov, M. Moliner and M. E. Davis, *ACS Catal.*, 2011, **1**, 408–410.
20 Y. Román-Leshkov, M. Moliner, J. A. Labinger and M. E. Davis, *Angew. Chem., Int. Ed.*, 2010, **49**, 8954–8957.
21 M. Choi, K. Na, J. Kim, Y. Sakamoto, O. Terasaki and R. Ryoo, *Nature*, 2009, **461**, 246–249.
22 D. Liu, A. Bhan, M. Tsapatsis and S. A. Hashimi, *ACS Catal.*, 2011, **1**, 7–17.
23 L. Emdadi, Y. Wu, G. Zhu, C. C. Chang, W. Fan, T. Pham, R. F. Lobo and D. Liu, *Chem. Mater.*, 2014, **26**, 1345–1355.
24 N. K. Mal, V. Ramaswamy, P. R. Rajamohanan and A. V. Ramaswamy, *Microporous Mater.*, 1997, **12**, 331–340.
25 W. E. Farneth and R. J. Gorte, *Chem. Rev.*, 1995, **95**, 615–635.
26 O. A. Abdelrahman, K. P. Vinter, L. Ren, D. Xu, R. J. Gorte, M. Tsapatsis and P. J. Dauenhauer, *Catal. Sci. Technol.*, 2017, **7**, 3831–3841.
27 W. Kim, X. Zhang, J. S. Lee, M. Tsapatsis and S. Nair, *ACS Nano*, 2012, **6**, 9978–9988.
28 S. F. Zhao, X. T. Yao, B. H. Yan, L. Li, Y. M. Liu and M. Y. He, *Chin. Chem. Lett.*, 2017, **28**, 1318–1323.
29 A. G. Machoke, I. Y. Knoke, S. Lopez-Orozco, M. Schmiele, V. R. R. Marthala, E. Spiecker, T. Unruh, M. Hartmann and W. Schwieger, *Microporous Mesoporous Mater.*, 2014, **190**, 324–333.
30 W. Park, D. Yu, K. Na, K. E. Jelfs, B. Slater, Y. Sakamoto and R. Ryoo, *Chem. Mater.*, 2011, **23**, 5131–5137.
31 K. S. W. Sing, D. H. Everett, R. A. W. Haul, L. Moscou, R. A. Rouquerol and T. Siemieniewska, *Pure Appl. Chem.*, 1985, **57**, 603–619.
32 M. Thommes, Textural Characterization of Zeolite and Ordered Mesoporous Materials by Physical Adsorption, in *Introduction to Zeolite Science and Practice*, ed. J. Cejka, H. van Bekkum, A. Corma and F. Schüth, Elsevier, 3rd edn, 2007, vol. 168, ch. 15, pp. 495–525, Stud. Surf. Sci. Catal.
33 R. Aiello, F. Crea, F. Testa, G. Demortier, P. Lentz, M. Wiame and J. B. Nagy, *Microporous Mesoporous Mater.*, 2000, **35**, 585–595.
34 S. L. Burkett and M. E. Davis, *J. Phys. Chem.*, 1994, **98**, 4647–4653.
35 M. A. Camblor, A. Corma, M. J. Díaz-Cabañas and C. Baerlocher, *J. Phys. Chem. B*, 1998, **102**, 44–51.
36 W. Kolodziejski, C. Zicovich-Wilson, C. Corell, J. Pérez-Pariente and A. Corma, *J. Phys. Chem.*, 1995, **99**, 7002–7008.
37 S. Maheshwari, C. Martínez, M. T. Portilla, F. J. Llopis, A. Corma and M. Tsapatsis, *J. Catal.*, 2010, **272**, 298–308.
38 D. Liu, A. Bhan, M. Tsapatsis and S. A. Hashimi, *ACS Catal.*, 2011, **1**, 7–17.
39 D. Coster, A. L. Blumenfeld and J. J. Fripiat, *J. Phys. Chem.*, 1994, **98**, 6201–6211.
40 J. P. Gilson, G. C. Edwards, A. W. Peters, K. Rajagopalan, R. F. Wormsbecher, T. G. Roberie and M. P. Shatlock, *J. Chem. Soc., Chem. Commun.*, 1987, 91–92.
41 P. Y. Dapsens, C. Mondelli, J. Jagielski, R. Hauert and J. Pérez-Ramírez, *Catal. Sci. Technol.*, 2014, **4**, 2302–2311.
42 G. Busca, *Catal. Today*, 1998, **41**, 191–206.
43 M. Trombetta and G. Busca, *J. Catal.*, 1999, **187**, 521–523.
44 M. Jiang and H. G. Karge, *J. Chem. Soc., Faraday Trans.*, 1996, **92**, 2641–2649.
45 S. Schallmoser, T. Ikuno, M. F. Wagenhofer, R. Kolvenbach, G. L. Haller, M. Sanchez-Sanchez and J. A. Lercher, *J. Catal.*, 2014, **316**, 93–102.
46 W. N. P. van der Graaff, C. H. L. Tempelman, E. A. Pidko and E. J. M. Hensen, *Catal. Sci. Technol.*, 2017, **7**, 3151–3162.
47 P. Bräuer, P. L. Ng, O. Situmorang, I. Hitchcock and C. D'Agostino, *RSC Adv.*, 2017, **7**, 52604–52613.
48 A. Platon and W. J. Thomson, *Ind. Eng. Chem. Res.*, 2003, **42**, 5988–5992.
49 S. Roy, K. Bakhmutsky, E. Mahmoud, R. F. Lobo and R. J. Gorte, *ACS Catal.*, 2013, **3**, 573–580.
50 M. Boronat, P. Concepción, A. Corma, M. Renz and S. Valencia, *J. Catal.*, 2005, **234**, 111–118.
51 L. Ren, Q. Guo, P. Kumar, M. Orazov, D. Xu, S. M. Alhassan, K. A. Mkhoyan, M. E. Davis and M. Tsapatsis, *Angew. Chem., Int. Ed.*, 2015, **54**, 10848–10857.
52 H. Liu, Y. Li, W. Shen, X. Bao and Y. Xu, *Catal. Today*, 2004, **93**, 65–73.
53 D. Ma, W. Zhang, Y. Shu, X. Liu, Y. Xu and X. Bao, *Catal. Lett.*, 2000, **66**, 155–160.
54 Q. Zhao, W. H. Chen, S. J. Huang, Y. C. Huang, H. K. Lee and S. B. Liu, *J. Phys. Chem. B*, 2002, **106**, 4462–4469.
55 W. E. Fameth, *Chem. Rev.*, 1995, **95**, 615–635.
56 M. Niwa and N. Katada, *Chem. Rec.*, 2013, **13**, 432–455.
57 N. Katada, H. Igi, J. H. Kim and M. Niwa, *J. Phys. Chem. B*, 1997, **101**, 5969–5977.
58 E. Sjöman, M. Mänttäri, M. Nyström, H. Koivikko and H. Heikkilä, *J. Membr. Sci.*, 2007, **292**, 106–115.
59 Y. Román-Leshkov, M. Moliner, J. A. Labinger and M. E. Davis, *Angew. Chem., Int. Ed.*, 2010, **49**, 8954–8957.

Supplementary Information for

Three-step cascade over one single catalyst: synthesis of 5-(ethoxymethyl)furfural from glucose over hierarchical lamellar multi-functional zeolite catalyst

Yuanyuan Bai,[abc] Lu Wei,[a,d] Mengfei Yang,[e] Huiyong Chen,[e] Scott Holdren,[f] Guanghui Zhu[g], Dat. T. Tran[h], Chunli Yao,[c] Runcang Sun,[c] Yanbo Pan[i] and Dongxia Liu*[a]

[a] *Department of Chemical and Biomolecular Engineering, University of Maryland, College Park, MD, 20742, USA*

[b] *National Engineering Lab for Pulp and Paper, China National Pulp and Paper Research Institute Co. Ltd., Beijing, 100102, China*

[c] *Beijing Key Laboratory of Lignocellulosic Chemistry, Beijing Forestry University, Beijing, 100083, China*

[d] *College of Materials Science and Engineering, Beijing University of Technology, Beijing 100124, PR China*

[e] *School of Chemical Engineering, Northwest University, Xi'an, Shaanxi, 710069, China*

[f] *Department of Chemistry and Biochemistry, University of Maryland, College Park, MD, 20742, USA*

[g] *School of Chemical and Biomolecular Engineering, Georgia Institute of Technology, Atlanta, Georgia, 30332, USA*

[h] *U. S. Army Research Laboratory, RDRL-SED-E, 2800 Powder Mill Road, Adelphi, MD, 20783, United States*

[i] *Department of Chemical and Biomolecular Engineering, University of Akron, Akron 44325, USA*

*Corresponding author:
Prof. Dongxia Liu
Email: liud@umd.edu
Phone: (+1) 301-405-3522
Fax: (+1) 301-405-0523

S1. Textural properties of MFI-Sn/Al catalysts

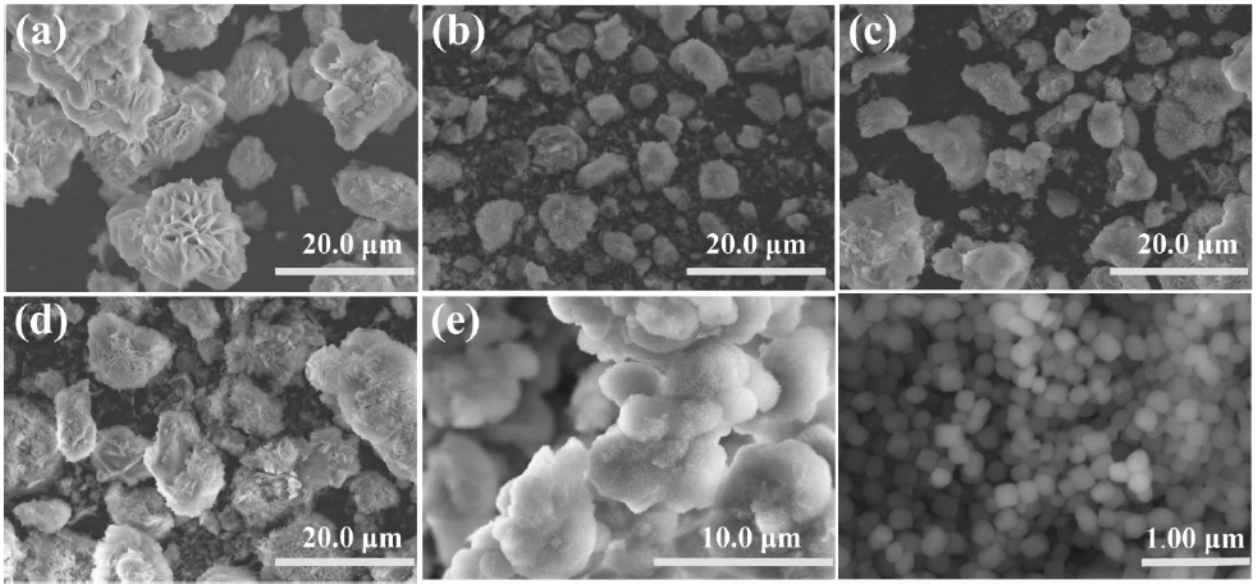

Fig S1. SEM images of (a) MFI-Sn/Al (100/100), (b) MFI-Sn/Al (100/50), (c) MFI-Sn/Al (100/25), (d) MFI-Sn/Al (50/50), (e) MFI-Sn/Al (∞/100) and (f) C-MFI-Sn/Al (100/100), respectively.

Table S1. Texual properties of the MFI-Sn/Al zeolite catalysts with different Sn/Al ratios and synthesis time determined from N_2 isotherms

Zeolite	V_{micro}[a] [$cm^3\ g^{-1}$]	S_{micro}[a] [$m^2\ g^{-1}$]	S_{ext}[a] [$m^2\ g^{-1}$]	V_t[b] [$cm^3\ g^{-1}$]	V_{meso}[c] [$cm^3 g^{-1}$]	S_{BET}[d] [$m^2\ g^{-1}$]
C-MFI-Sn/Al (100/100)	0.144	317	196	0.667	0.523	513
MFI-Sn/Al (50/50)	0.078	150	197	0.488	0.410	347
MFI-Sn/Al (100/25)	0.107	254	221	0.650	0.543	474
MFI-Sn/Al (100/50)	0.108	255	198	0.548	0.440	453
MFI-Sn/Al (100/100)	0.093	215	191	0.470	0.377	406
MFI-Sn/Al (∞/100)	0.092	180	374	0.859	0.767	554

[a] Determined from t-plot method
[b] Determind by NLDFT method
[c] $V_{meso}=V_t-V_{micro}$
[d] Determined from multi-point Brunauer, Emmett, a Teller (BET) method

Table S2 Concentration of Sn and Al in MFI-Sn/Al zeolite catalysts.

Zeolite	MFI-Sn/Al (100/100)	MFI-Sn/Al (100/50)	MFI-Sn/Al (100/25)	MFI-Sn/Al (50/50)	C-MFI-Sn/Al (100/100)	MFI-Sn/Al (∞/100)
Si/Sn[a]	100	100	100	50	100	∞
Si/Al[a]	100	50	25	50	100	100
Si/Sn[b]	75	51	53	31	70	∞
Si/Al[b]	67	32	20	37	65	72

[a] Calculated from synthesis recipe; [b] Determined from elemental analysis (ICP-AES).

S2. Effect of zeolite acidity on EMF synthesis from glucose over MFI-Sn/Al catalysts

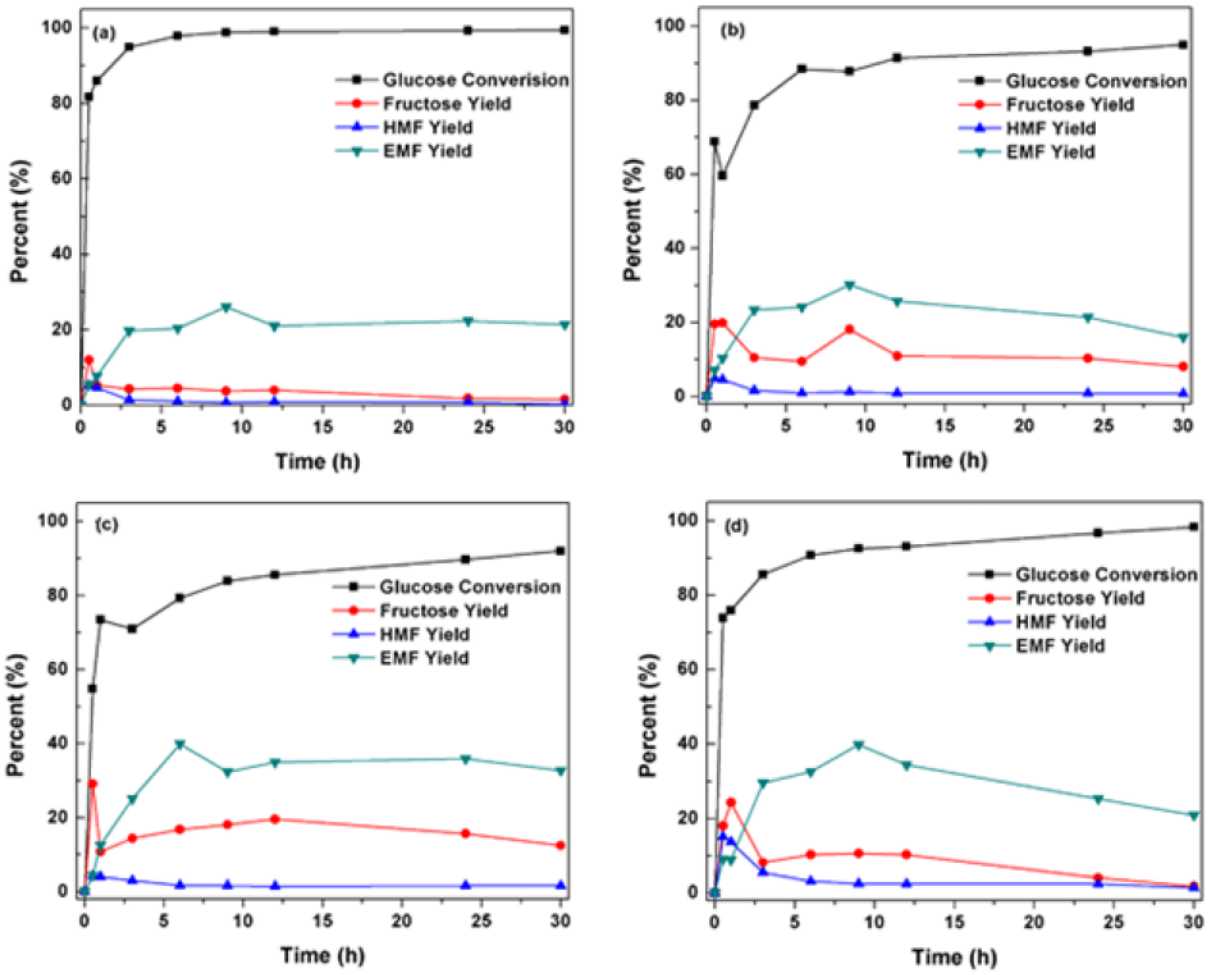

Fig. S2 Catalytic conversion of glucose over MFI-Sn/Al zeolite catalysts ((a) MFI-Sn/Al (100/100); (b) MFI-Sn/Al (100/50); (c) MFI-Sn/Al (100/25); (d) MFI-Sn/Al (50/50)) as a function of reaction time at 413 K.

S3. Effect of carbohydrate type on EMF synthesis over MFI-Sn/Al catalyst

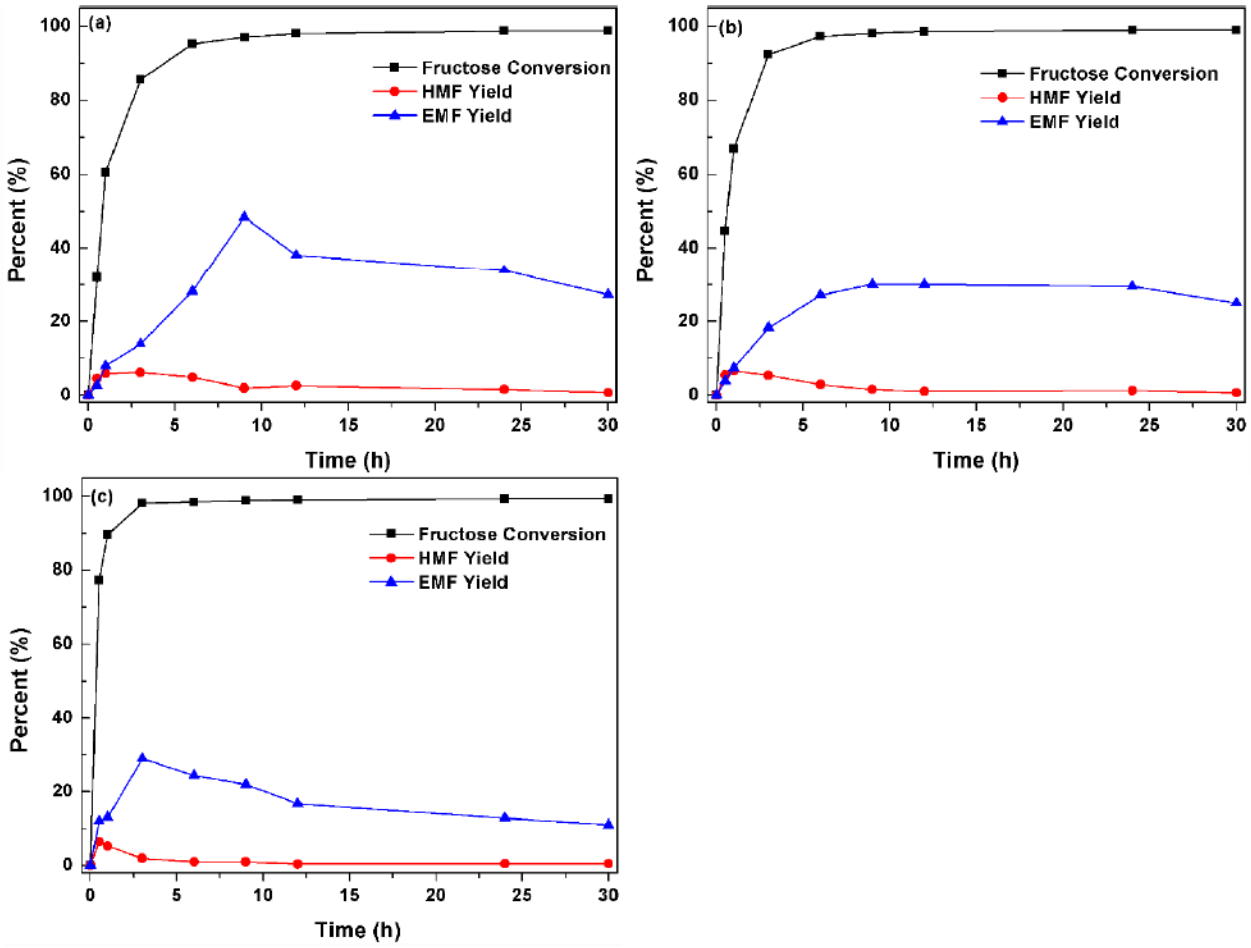

Fig. S3 Catalytic conversion of fructose over MFI-Sn/Al (100/100) versus reaction time at temperature of (a) 398 K, (b) 406 K, and (c) 413 K, respectively.

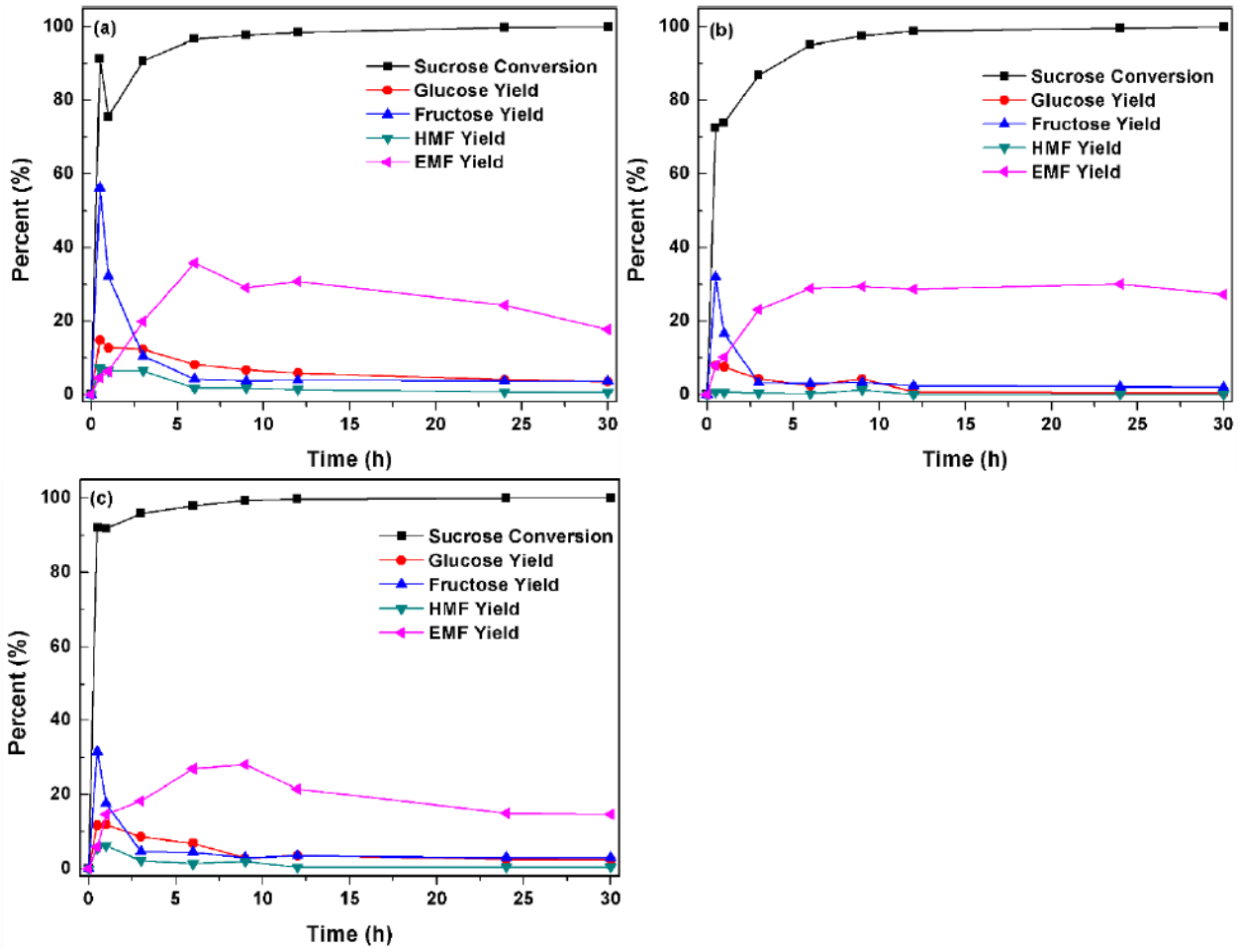

Fig. S4 Catalytic conversion of sucrose over MFI-Sn/Al (100/100) at different tempatures: (a) 398 K, (b) 406 K, and (c) 413 K;

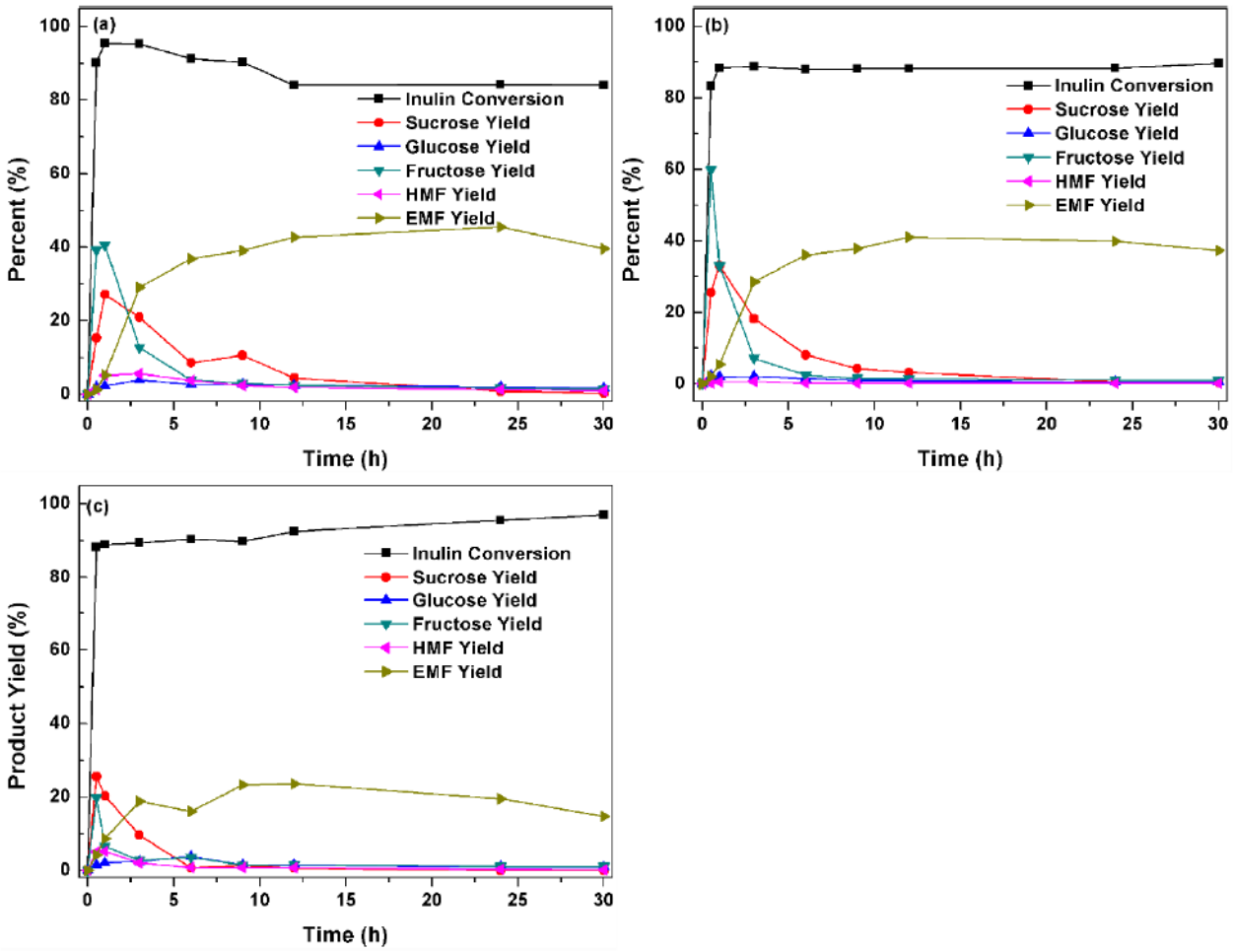

Fig. S5 Synthesis of EMF from inulin by MFI-Sn/Al (100/100) at different tempatures: (a) 398 K, (b) 406 K, and (c) 413 K.